*Physics – Uspekhi* **67** (1) 3 – 21 (2024) 

*REVIEWS OF TOPICAL PROBLEMS* PACS numbers: **07.57. – c,** 42.30.Wb, **84.40. – x**

# Optical-to-terahertz switches: state of the art and new opportunities for multispectral imaging

D S Ponomarev, A E Yachmenev, D V Lavrukhin, R A Khabibullin,
N V Chernomyrdin, I E Spektor, V N Kurlov, V V Kveder, K I Zaytsev

DOI: https://doi.org/10.3367/UFNe.2023.07.039503

## Contents



**Abstract. Compact and cost-effective spectrometers and imaging systems in the terahertz (THz) frequency range based on optical-THz photoconductive converters of ultrashort laser pulses (photoconductive antennas — PCAs) are actively being developed and widely used to solve fundamental and applied problems in a variety of fields of science and technology. This high activity of research and development is associated with the PCAs' reliability and compact size, the easy scalability of a single element to 1D and 2D arrays, and PCAs' ability to provide a wide spectral range and high dynamic range of recorded THz signals without cooling. Recently, systems for multi-pixel detection of THz radiation based on matrix PCA detectors, designed to greatly increase the speed of THz imaging, have been of particular interest. This review presents the latest trends in the development of PCA-based THz devices, PCA-based methods of THz pulsed spectroscopy and imaging, as well as alternative approaches to THz pulse recording and THz imaging.**

**D S Ponomarev** [1, 2, 3, *], **A E Yachmenev** [1], **D V Lavrukhin** [1, 2], **R A Khabibullin** [1, 3], **N V Chernomyrdin** [2], **I E Spektor** [2], **V N Kurlov** [4], **V V Kveder** [4], **K I Zaytsev** [2]
[1] V G Mokerov Institute of Ultra High Frequency Semiconductor Electronics, Russian Academy of Sciences, Nagornyi proezd 7, 117105 Moscow, Russian Federation
[2] Prokhorov General Physics Institute, Russian Academy of Sciences, ul. Vavilova 38, 119333 Moscow, Russian Federation
[3] Moscow Institute of Physics and Technology (National Research University), Institutskii per. 9, 141701 Dolgoprudnyi, Moscow region, Russian Federation
[4] Osipyan Institute of Solid State Physics, Russian Academy of Sciences, ul. Akademika Osipyana 2, 142432 Chernogolovka, Moscow region, Russian Federation
E-mail: [*] ponomarev_dmitr@mail.ru

Received 24 November 2022, revised 4 July 2023
*Uspekhi Fizicheskikh Nauk* **194** (1) 2 – 22 (2024)
Translated by V L Derbov

**Keywords:** THz radiation, sources and detectors of THz pulses, semiconductors, THz imaging, time-domain THz spectroscopy, photoconductive antennas, low-temperature grown GaAs, InAlAs/InGaAs superlattice heterostructures, ultrashort pulse generation, near-field THz microscopy, solid-immersion microscopy, THz tomography, multispectral THz imaging

## 1. Introduction

Historically, the terahertz (THz) frequency region, adjacent to the microwave and infrared (IR) regions on the scale of electromagnetic waves, was called the THz gap, because there were no efficient sources or detectors of THz radiation, nor were there elements of THz beam control. Today, it is accepted to consider the THz range as corresponding to frequencies of 0.1–10 THz or wavelengths of 0.03–3 mm [1]. THz electromagnetic radiation has a number of unique features. The frequency dependence of THz complex permittivity of a medium carries information on low-frequency molecular vibrations and structural properties of the substance. THz radiation is sensitive to water content and the state (free or bound) in water-containing systems, including biological tissues. THz radiation can penetrate through nonpolar dielectric materials, such as paper, plastic, cloth, wood, and ceramics, which are opaque in the visible and IR ranges. THz spectroscopic and imaging systems possess better resolution than their counterparts in the radio and millimeter-wave ranges. In recent decades, these features of THz waves have stimulated the development of THz engineering, designing a new high-efficiency elemental base for THz optoelectronics, creating unique laboratory research facilities, as well as commercial spectroscopic and imaging systems.

Progress in THz time-domain spectroscopy and imaging is inextricably linked with improvement in the existing elemental base of the THz range. Among the sources and detectors of THz radiation, photoconductive antennas

(PCAs) have become the most universal component of up-to-date broadband THz spectroscopic and imaging systems over recent decades. The still high publication activity is associated with important competitive advantages of PCA-based THz time-domain spectrometers. In particular, a PCA source excited by near-IR femtosecond laser pulses is capable of providing a bandwidth of 100 GHz – 6 THz [2–4], and even more [5]; a coherent PCA detector can record the profile of a THz wave packet in the time domain or simultaneously record the spectral phase and amplitude of a THz wave in the frequency domain. By using a PCA in THz spectrometers, it turns out to be possible to implement the mean power of a THz beam of up to $\approx 600$ μW [6], as well as to achieve what is to date a record-breaking optical-to-THz power conversion efficiency of $\approx 7.5\%$ [7]. Although there are many alternative mechanisms of THz generation and detection and devices implementing them (including generators based on electrons accelerated to relativistic velocities [8], backward-wave tubes [9, 10], free-electron lasers [10, 11], Gunn diodes [12], avalanche transit time and resonance tunneling diodes [13], and quantum cascade lasers [14, 15]), all of them are much less widespread than PCAs due to their high cost, their poor ergonomics, and (sometimes) the necessity to operate at cryogenic temperatures.

This is exactly why in this review we focus on PCAs and PCA-based methods of THz imaging. We will consider the main methods of generating and detecting THz radiation with an emphasis on PCAs as most often used in THz pulsed systems. We will describe the approaches to efficiency improvement and the results achieved. We will consider the basic principles of time-domain THz spectroscopy and imaging. We will consider the classical methods of THz imaging with diffraction-limited resolution, including confocal THz microscopy, as well as methods of near-field imaging, overcoming the Abbe limit (for focusing in free space) and providing a resolution of up to $10^{-3}\lambda$ [16]. The near-field microscopy method based on solid immersion will be considered, which allows increasing the spatial resolution of an optical system.

## 2. Principle of operation of optical-to-terahertz switches

The processes of pulsed radiation generation and detection can be implemented based on various physical principles [17], among which we will select and describe below four types.

### 2.1 Acceleration of charge carriers in semiconductors

With the progress in femtosecond laser techniques [18] and the appearance of new photoconductors, PCAs became more manufacturable, efficient, and widespread devices to generate and detect THz radiation. The approach to generating and detecting THz pulses based on the accelerated motion of photoexcited carriers in a semiconductor was first proposed by D Auston et al. in Refs [19, 20], where silicon on a sapphire substrate was used as a photoconductive medium. The PCA is formed by two metallic electrodes separated by a small gap on the surface of a semiconductor. When the PCA is excited by an ultrashort ($\leqslant 100$ fs) laser pulse with a photon energy exceeding the semiconductor band gap, nonequilibrium photoexcited charge carriers are formed in the gap, and the antenna almost instantly moves to a conducting state.

The generation of THz radiation in a PCA is a rather complex process; therefore, in the literature, various descriptions are found. For example, in Ref. [21], the following formulation is given: under exposure to a bias electric field applied to the PCA, a transit current is formed, which, due to the short lifetime of nonequilibrium carriers, in the course of damping excites electromagnetic field oscillations at GHz and THz frequencies. However, the process of generating THz radiation is not only determined by the acceleration of nonequilibrium charge carriers in the PCA bias field. A more detailed description presented in Ref. [22] is that the transit current formation in a PCA implies the optical generation of hot electrons and holes, their fast thermalization, the ballistic acceleration of carriers, and a burst of the drift velocity in a subpicosecond time interval. This description removes the apparent contradiction associated with the fact that, in order to generate radiation, it is necessary that the lifetime of charge carriers in the photoconductor be short. Indeed, efficient enough radiation generation is possible using photoconductive materials with a lifetime $> 100$ ps [23, 24]; the efficiency of generating radiation in PCA is directly proportional to the electron mobility in the photoconductor and the bias voltage [25]. Hence, to increase it, a high-mobility material is required; at the same time, to safely increase the bias voltage, a high resistance of the material is required. Simultaneous satisfaction of both requirements is rather problematic, and the solution is usually a compromise combination of these parameters. High-resistance materials, such as LT-GaAs, ensure a compromise between the mobility and the lifetime: having a specific resistance of $10^7\ \Omega\ \mathrm{cm}^{-1}$ [26], they provide sufficiently high mobility within 100–300 $\mathrm{cm}^2\ \mathrm{V}^{-1}\ \mathrm{s}^{-1}$. It is important to note that, in contrast to PCA sources, to detect THz radiation, it is preferable to use materials with a short carrier lifetime in order to reduce the thermal noise of the PCA detector [3, 27]. A schematic diagram of a PCA source and its operation as part of a time-domain THz spectrometer are illustrated in Fig. 1.

The existing approaches to increasing PCA efficiency are related to modifying optical and transport properties of the semiconductor material and developing new PCA topologies and designs. Let us describe the main areas of PCA optimization.

Significant progress in the development of THz PCAs occurred with the onset of using LT-GaAs-based semiconductors. In combination with Ti:sapphire femtosecond lasers, PCA sources and detectors became the main components of pulsed THz systems. The growth of GaAs layers by molecular beam epitaxy (MBE) at a low temperature under the conditions of excess arsenic flow leads to the introduction of excess As atoms into the GaAs crystal lattice. During the subsequent postgrowth annealing of the sample under increased temperature, the formation of As precipitates occurs, as a result of which LT-GaAs acquires the necessary properties, namely, a short lifetime of photoexcited electrons ($< 1$ ps) in combination with sufficient mobility (100–200 $\mathrm{cm}^2\ \mathrm{V}^{-1}\ \mathrm{s}^{-1}$) [28, 29]. Other methods of modifying the properties of bulk materials are implantation of GaAs with heavy or light $\mathrm{As}^+/\mathrm{O}^+/\mathrm{H}^+/\mathrm{C}^+$ ions [30, 31] or radiation damage of the crystal lattice of GaAs [32], InP [33], GaAsBi [34].

Currently, various multilayer structures have proven themselves well in THz spectroscopy systems [35], in particular, superlattice heterostructures [4, 36]. The first structures of this type to be used were those in which many layers of ErAs quantum dots were embedded in the bulk of GaAs [37]. With a correct choice of the growth conditions, a

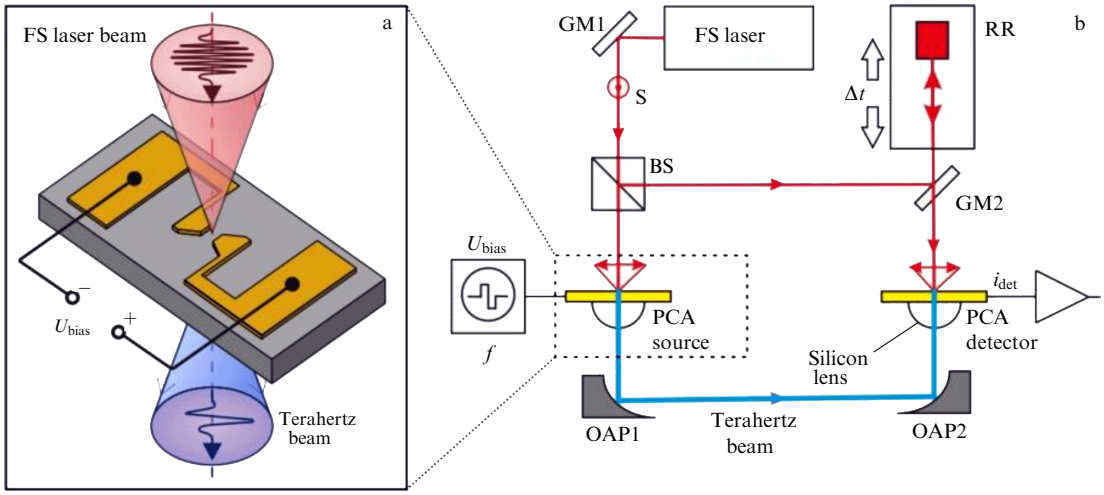


**Figure 1.** Schematic diagram of a PCA source (a) and its operation in a THz time-domain spectrometer (b). Optical paths of the laser and THz beams are shown in red and blue, respectively. GM — dielectric mirror; BS — beam splitter; RR — optical delay line with a movable corner reflector; OAP — off-axis parabolic mirror; PCA — photoconductive antenna.

moderate mobility of carriers is retained and the precipitates or quantum dots created in the course of ErAs growth form recombination centers in the middle of the GaAs band gap. Embedding ErAs layers into the superlattice structure of In(Al)GaAs made it possible to obtain a record-breaking dynamic range of 78 dB with a generation bandwidth up to $\approx 3.65$ THz at the laser excitation wavelength of 1550 nm [38]. In Ref. [39], the authors report a mean generated power of 164 μW of radiation from an ErAs:In(Al)GaAs-based PCA source with a mean laser pump power of 42 mW and bias voltage of 200 V.

Another approach is to form InAs quantum dots on the GaAs surface. Such quantum dots are produced as a result of relaxation of elastic stresses, arising due to a strong mismatch of lattice parameters in epitaxial layers. Their presence in the matrix of the parent substance not only serves to reduce the lifetime when maintaining the mobility high enough, but also allows using femtosecond laser pumping with the central wavelength in the range of 1.0–1.3 μm [40, 41]. Similar to ErAs layers, photoconductors with InAs quantum dots can be used to generate THz radiation [42–44]. In one recent paper, it was shown that traditional PCAs based on such quantum dots preserve efficiency up to the mean power of laser excitation (photoconductor irradiance) of $\approx 1.1$ mJ cm$^{-2}$, which is 20 times higher than the LT-GaAs pump limit.

The demand for compact THz systems and progress in fiber femtosecond lasers with a central wavelength of 1550 nm made it relevant to develop photoconductors with a band gap that permits absorption of a photon with the appropriate (smaller) quantum energy. $In_{0.53}Ga_{0.47}As$ is such a photoconductive materials; however, it is not suitable in its initial form for use in PCA-based radiation sources because of the long lifetime of photoexcited charge carriers and excessive dark current. To optimize its properties, various approaches are being developed: doping low-temperature InGaAs (LT-InGaAs) [46], ion implantation [47, 48], and creating beryllium-doped superlattice LT-InGaAs/InAlAs heterostructures [49]. The best result when using beryllium in LT-InGaAs/InAlAs has been obtained in Ref. [50], where the gradient doping of InAlAs layers has provided a more rapid capture of photoexcited charge carriers using traps, keeping the mobility unchanged. The obtained PCAs were characterized by a spectral bandwidth of generation up to 6 THz and dynamic range of 70 and 55 dB at frequencies of 3 and 4 THz, respectively.

The authors of Ref. [51] proposed a design of a superlattice heterostructure of undoped 'high-temperature' (grown at a temperature usual for MBE growth) InGaAs/InAlAs layers. The mobility in them reaches 3000 cm$^2$ V$^{-1}$ s$^{-1}$ thanks to the spatial separation of perfect crystal layers of InGaAs (with high mobility) and a defect layer of InAlAs (responsible for the recombination of photoexcited carriers at composition inhomogeneities because of microalloy scattering). Using this structure, the mean output power of $\approx 64$ μW was obtained from a PCA-based source with a mean laser pump power of $\approx 32$ mW, which corresponds to an optical-to-THz conversion efficiency two orders of magnitude higher than in superlattice heterostructures based on beryllium-doped LT-InGaAs/InAlAs [52]. An even greater increase in the efficiency of this structure can be achieved by introducing elastic stresses in the layers, due to which the roughness of heterointerfaces and the rate of charge carrier scattering on them increase, while the mobility in the bulk crystal lattice is preserved [53].

In Ref. [2], it is proposed that InGaAs be doped with iron, acting as a deep acceptor impurity and forming recombination levels in the middle of the InGaAs band gap. A mean output power of the corresponding PCA at the level of $\approx 75$ μW was obtained, the generated bandwidth reached 6 THz, and the dynamic range amounted to 95 dB. A detailed investigation of photoexcited electron dynamics in InGaAs:Fe has shown that the photoelectron lifetime reaches 0.23 ps [54]. A promising idea is to dope InGaAs with rhodium (Rh), which, like iron, forms deep acceptor levels, but at the same time possesses a lower diffusion coefficient and has a smaller tendency to cluster formation at higher doping concentrations [55]. The characteristics of InGaAs:Rh surpass those of practically all known analogs: the lifetime of photoexcited charge carriers is reduced to $\approx 100$ fs, the mobility being $\approx 1000$ cm$^2$ V$^{-1}$ s$^{-1}$ [56]. This allowed creating on its basis a PCA detector with a record-breaking dynamic range of 105 dB and the high-frequency boundary of the operating spectral range up to 6.5 THz [3], as well as a PCA source with a mean output power of $\approx 637$ μW,

the mean power of laser excitation being ≈ 28 mW [6]. One promising way of THz generation by PCAs is to use topological insulators based on $Bi_2Se_3$ and $Bi_{2-x}Sb_xTe_{3-y}Se_y$ films [57].

Along with the photoconductor material, the spectral and energy characteristics of a PCA are determined by the chosen topology of electrodes. Depending on the width of the gap between the electrodes, the categories of wide-aperture and dipole PCAs can be distinguished. In dipole PCAs, the gap between the electrodes is smaller than the THz wavelength, and in wide-aperture ones it exceeds the THz wavelength (by up to two orders of magnitude) [58–60]. Increasing the operating gap region in wide-aperture PCAs was an attempt to raise the saturation threshold and output power of THz radiation. However, to create the corresponding electric field strength in a large gap, a voltage supply of up to 45 kV is required [61], which, together with the known effect of bias field screening by the emitted THz pulse [59, 62], has limited the use of such PCAs. The most successful approach to increasing the THz radiation generation power is the use of easily scalable large-format PCAs, comprising an array of interdigital electrodes. Initially implemented by Yoneda et al. [63], large-scale PCAs allow making an emitting element of arbitrary area and using a high-power optical pump without impairing the generation efficiency because of charge screening effects and thermal breakdown [64–67]. The choice of antenna topology also makes it possible to control the frequency-angular (spatial) distribution of the generated THz wave [68–70]. Among dipole PCAs, the following topologies remain the most common: a microstrip antenna (consisting of parallel conductors), dipole, bow tie, and logarithmic spiral (Fig. 2). The choice of particular topology is determined by the area of PCA application. For example, a dipole topology may be designed for a specific resonant frequency, while a logarithmic spiral provides the maximum bandwidth.

When detecting radiation, no bias voltage is applied, and the charge carriers in the antenna gap are accelerated by the electric field of the incident THz wave forming the signal current [71–73]. To study the polarization characteristics of the THz radiation, PCA detectors with crossed electrodes have been proposed [74, 75]; for studying spatial characteristics, it is linear and matrix PCA detectors [76–78].

Another line of study aimed at improving the PCA characteristics is increasing the efficiency of optical-to-THz conversion of energy in the antenna. The existing approaches are, first, based on enhancing the localization of the exciting optical radiation in the PCA gap [79, 80]. This principle can be most effectively implemented by forming a metasurface in the PCA gap. Various types of metasurfaces for PCAs are considered in reviews [81–83]. In the present paper, we will briefly consider the main results for PCAs with dielectric and metallic metasurfaces.

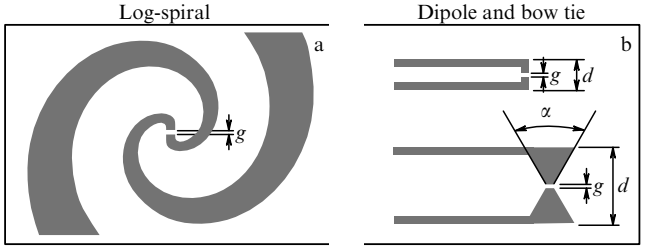


**Figure 2.** Schematic diagrams of widespread topologies of PCA electrodes: (a) logarithmic spiral (log-spiral); (b) dipole (top), and bow tie (bottom). Here, $g$ is the gap between electrodes; $d$ is the length of electrodes; $\alpha$ is the angle of flare.

A metallic (plasmonic) metasurface is formed in the PCA gap by subwavelength metallic elements, producing a certain distribution of the exciting laser field on their shadow side (on the surface and in the bulk of the photoconductor) [84]. Frequently, the role of such elements is played by 1D or 2D plasmonic gratings. The increase in THz generation efficiency is related to the local enhancement of the exciting laser field in addition to the metallic elements due to the formation of plasmonic modes [82, 85, 86]; this local field becomes more intense than the incident light wave field by orders of magnitude [87]. One of the most efficient metallic metasurface topologies has been proposed in Ref. [88]. It is formed by an array of interdigital electrodes of subwavelength size (plasmonic grating) connected with the master PCA electrodes. An optical pump pulse is incident on the lattice with a positive potential so that practically all photoexcited charge carriers created in the immediate vicinity of the electrodes contribute to the photocurrent. A 50-fold increase in the power of THz generation in a PCA source based on LT-GaAs with a plasmonic grating compared to the analogous PCA without a lattice and a 30-fold increase in the sensitivity of a plasmonic PCA detector were demonstrated. A record-breaking optical-to-THz conversion efficiency of ≈ 7.5% in a PCA source was obtained in Ref. [7]. This was made possible by using a three-dimensional plasmonic grating embedded in the semiconductor to a depth of 400 nm. This allowed localizing practically all the photoexcited electrons near the lattice electrodes in a subpicosecond time interval. The mean power of the generated THz radiation amounted to ≈ 105 μW with a mean laser pump power of only ≈ 1.4 mW.

In 2019, a Russian source of broadband THz radiation (0.1–4.5 THz) was developed, in which a high-aspect plasmonic grating with a lattice height of 100 nm and height-to-period ratio of 0.5 was first used (Fig. 3) [90]. Such a lattice simultaneously provides a strong laser field localization at the photoconductor and a brightening of its surface due to the excitation of canalized plasmonic modes. In 2022, the design of the lattice was improved by increasing the aspect ratio to 0.8 (the lattice geometry was calculated to maximize the coefficient of laser pump energy transmission through the lattice); in this case, its height was already 170 nm, thus forming a narrow-slit resonator, in which at least one plasmonic mode of higher order was excited. This caused an increase in the dynamic range (i.e., the signal-to-noise ratio) of the THz time-domain spectrometer based on such an antenna by 10 dB and an almost 10-fold increase in the mean power of the generated THz beam [89]. The total power in the range of 0.1–4.5 THz amounted to 5 μW with a mean laser excitation power of 10 mW and bias voltage of 5 V.

Cross-shaped plasmonic elements allow implementing a polarization-insensitive THz PCA detector [91]. For a further increase in PCA efficiency, individual antennas with a plasmonic grating can be collected into 1D or 2D arrays of many elements [92] or form a single large-area element [66]. The addition of a Bragg grating (dielectric mirror) under the functional layers of undoped GaAs in combination with a PCA with a plasmonic grating on the structure surface allows designing a plasmonic resonator, providing efficient absorption of a femtosecond laser pump pulse [67]. A layer of GaAs only 170 nm thick with a relatively high mobility of charge

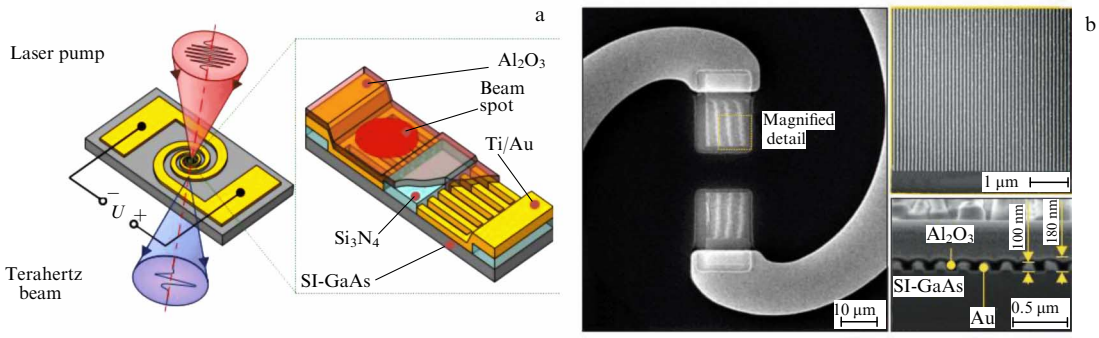


**Figure 3.** THz PCA source with a plasmonic grating [90]: (a) PCA designs with logarithmic spiral electrodes (left) and a plasmonic grating in the gap between electrodes (right); (b) image of the plasmonic grating obtained by means of scanning electron microscopy, including a general view of the gap, a magnified image of the plasmonic grating (top view), and an image of the plasmonic grating section (side view).

carriers is used as a photoconductive layer. This means that, during a THz pulse (1–2 ps), all photoexcited carriers will contribute to the photocurrent and, therefore, the layer will be completely depleted. Results of studying a PCA detector based on a plasmonic resonator showed that, in the spectral range of 0.1–4.5 THz, it enables a dynamic range of 100 dB with a mean pump power of 5 mW, which corresponds to results for detectors based on a photoconductor with an ultrashort lifetime. Using a similar approach, but without a resonator, a record-breaking dynamic range of 122 dB and spectral range of more than 3.6 THz were demonstrated with a mean laser pump power of 10 mW [93]. A layer of $In_{0.53}Ga_{0.47}As$ only 200 nm thick was used and the topology of PCA electrodes was previously optimized to support high impedance and a low level of Johnson–Nyquist noise. Plasmonic metasurfaces can be calculated and used not only for the optical range but also for the THz range [94, 95]. Due to the resonant nature of the interaction between the metasurface and the incident wave field, this enables tuning the PCA to amplify specified spectral bands and even individual frequencies in the generated THz spectrum [95].

The second type of metasurface is dielectric structures. Although initially dielectric coatings were applied to the PCA surface as blooming layers [7, 93], with time, it became clear that dielectric nanostructures based on materials with a high refractive index can also be used for subwavelength localization of the exciting laser IR radiation. In contrast to metallic metasurfaces — often having a relatively small transmission coefficient and being laborious to produce and nondurable in exploitation [96] — dielectric structures are free of these drawbacks; moreover, they have no ohmic losses in principle [97].

The concept of an all-dielectric metasurface in application to PCA detectors was proposed in Ref. [98]. The metasurface was a system of parallel strips of subwavelength size produced by LT-GaAs etching. A PCA detector based on a structure with dielectric metasurface produces photocurrent an order of magnitude greater than a similar PCA without a metasurface at the mean laser pump power of $P_{opt} \sim 0.5$ mW. Later, the same authors proposed an ideally absorbing laser radiation dielectric metasurface, represented by an array of Mie resonators [99]. It was shown that the resonators formed in the bulk of the GaAs photoconductor support two strongly coupled degenerate magnetic modes. The magnetic moment of one of them is normal to the photoconductor surface and the other one lies in its plane. Simultaneous excitation of both modes gives rise to nearly total absorption of laser pump radiation at a wavelength of 800 nm, and the PCA detector demonstrates a signal-to-noise ratio of $\sim 10^6$ at an extremely low mean pump power of $\approx 100$ μW. Finally, in Ref. [100], a PCA source was studied with an all-dielectric metasurface in the form of a subwavelength nanolattice produced directly on a GaAs semiconductor between the microstrip electrodes of the antenna. Optimization of the nanolattice dimensions made it possible to bloom the photoconductor, reducing the laser pump reflection to 2.53%, and to increase the power of THz generation 3.92 times in the range of 0.05–1.6 THz.

There are many fewer experimental studies of dielectric metasurfaces than theoretical ones, in which a variety of compositions, designs, and topologies of dielectric elements are considered [101–103]. This is due to serious difficulties etching single crystals to obtain elements of the specified shape and size.

Note that THz pulse generation in photoconductors is also possible without a bias field at the expense of the Dember photovoltaic effect [104–108], the presence of a built-in electric field in the near-surface layer of a semiconductor [109], and the excitation of a leaky mode in vertical filamentous crystals of GaAs [110, 111]. The power of generated THz radiation in the above approaches is small compared to PCA [68].

Theoretical modeling aimed at describing the ultrafast dynamics of carriers in surface emitters was carried out in Ref. [112] using the 3D semiclassical Monte Carlo model. The results of the modeling show that, in the case of InAs photoexcitation, the main mechanism of generating THz radiation is the Dember effect, whereas for GaAs the generation process due to the built-in electric field prevails. Similar work on calculating the Dember photo EMF and THz generation in InAs upon excitation of the semiconductor, including by high-energy radiation with effects of intervalley scattering, was carried out in Ref. [23]. It was shown that, when exciting *n*-InAs by laser pulses with a duration of 100 fs and a quantum energy of 1.55 eV, the photo EMF reaches the maximum value nearly 100 fs after the photoexcitation process. Note that the mechanism of photo EMF emergence in this case has a reactive nature and is caused by the asymmetric expansion of electrons upon their reflection from the semiconductor surface.

Wafers of GaAs 0.3–0.5 mm thick, which attenuate the radiation at frequencies higher than 5 THz due to absorption by optical phonons, are most often used as substrates for the formation of photoconductive layers. To increase the PCA

bandwidth, technologies are being developed for transferring the photoconductive layer to an alternative substrate of nonpolar material [113], of the epitaxial growth of photoconductors on silicon [114] or germanium [5, 115] substrates. For example, Ref. [5] shows the possibility in principle of obtaining THz generation with a spectral width up to 70 THz.

There are a number of physical processes that reduce the efficiency of THz generation in PCAs. First, screening effects lead to the saturation of power. They include radiation screening, i.e., a decrease in the applied bias field at the expense of the generated THz field [62, 116, 117] and the screening effect related to the redistribution of the spatial charge formed after photoexcitation, which reduces the bias field (Coulomb screening) [59]. In wide-aperture PCAs, Coulomb screening is less manifested due to more homogeneous photoexcitation and a large surface area. In Ref. [117], it is quantitatively shown that, in wide-aperture PCAs with an optical pump spot diameter $> 100$ μm, the efficiency of optical-to-THz conversion is almost 100 times higher than that in a dipole PCA with a pump spot diameter of 7 μm. A group of nonlinear optical effects can be distinguished among the effects affecting PCA efficiency. These include the Burstein–Moss effect related to the shift of the conduction band edge because of saturation by nonequilibrium carriers upon photoexcitation. The characteristic time for filling the conduction band is from 1 ps in GaAs to 1.7 ps in superlattice GaAs/AlGaAs structures [118], which can reduce the coefficient of absorption of the photoconductive layer in a PCA. In addition, the correct calculation of a PCA based on GaAs (LT-GaAs) grown at a low temperature requires taking into account the components related to light-induced transparency [119, 120]. This effect manifests itself at an ultrashort time interval of $< 1$ ps and is caused by the presence of trap energy levels in the band gap of LT-GaAs. The change in the LT-GaAs refractive index with the self-induced transparency taken into account can exceed 0.1 [119].

It is also necessary to consider the effects of delay and nonstationarity of the electromagnetic interaction between the current of photoexcited charge carriers and the electric field of the generated electromagnetic wave. Using the self-consistent solution of the nonequilibrium Boltzmann equation and Maxwell equations, the authors of Ref. [121] established the fundamental role of an electron-hole plasma bunch created as a result of photoexcitation and moving in the transverse electric field. The generation of THz radiation is possible at moments of the emergence and decay of this bunch in the form of single or double pulses, depending on the interaction with the boundaries of the semiconductor photoconductive layer.

Since the bottom of the conduction band in GaAs has a multivalley structure with a fairly small energy difference between the minima of Γ, L, and X valleys [122], the excess energy of electrons can cause them to be projected to higher-energy valleys [123, 124]. Due to the greater effective mass and lower mobility of carriers in L and X valleys, this process can substantially affect the dynamics of photoexcited electrons and the efficiency of THz generation, depending on the emitter type. In Ref. [125], the effect of the excess energy received by electrons under pumping three types of semiconductors with different band gap widths and mobility on the efficiency of surface THz generation is studied by modeling. It is shown that the value of the initial kinetic energy received by the electrons is of paramount significance, because ballistic transport is the main mechanism of THz generation in surface emitters. This was also experimentally confirmed in Ref. [104], where, at the same pump energy, the surface THz generation of radiation was studied in samples of $In_xGa_{1-x}As$ with $x$ varying from 0.3 to 0.7. Note that, in the case of PCA, the carriers can acquire excess energy not only when absorbing an optical pump pulse but also during drift in the bias field applied to the PCA electrodes, which can exceed $10^4$ V cm$^{-1}$. In this case, the intervalley scattering of carriers leads to a decrease in the photocurrent because of deceleration of carriers that find themselves in high-energy valleys and to the appearance of a negative peak in the THz wave packet [126].

Several models have been developed to theoretically describe the THz generation process in PCAs. The first group of papers is based on the representation of a PCA source as a semiconductor wafer with a surface current oscillating during the optical pulse. Within the framework of this model, the electromagnetic field emitted into free space is determined using the boundary conditions, as well as through the relation with the surface current [116, 127]. Since the depth of optical pulse absorption in a semiconductor is comparable to the wavelength, this approach is not correct enough. The basic models to describe THz generation in PCAs are those based on the solution to the system of drift and diffusion equations [128, 129], and the Drude–Lorentz theory of charge carrier transport [130, 131]. In Ref. [132], the semiclassical Monte Carlo model from Ref. [112] was extended to describe the THz generation process in PCAs. As a result, the authors identify two regimes with different mechanisms to limit generation power:

- through pumping with ultrashort pulses with a duration of $< 40$ fs, the limiting is due to the Gaussian distribution of energy in the pulse;
- for pulses with a duration of $> 40$ fs, the dominant mechanism is Coulomb screening.

The authors of Ref. [133] in their model considered effects associated with 'hot' carriers under the maximum possible power of laser excitation and magnitude of the PCA bias field. The model of energy transport balance was used to describe the effects of saturation and overshoot of photocurrent. It is also necessary to note theoretical studies on describing the THz generation process in photomixers [134, 135].

### 2.2 Generation of terahertz radiation in p–i–n diodes

p–i–n photodiodes are also often used as semiconductor THz radiators. They cannot surpass semiconductor PCAs in the pulsed mode because the power of THz generation is not high, although their efficiency can exceed that of p-InAs PCA in the regime of a surface THz emitter for a power density of $< 0.7$ μJ cm$^{-2}$ [136]. Thanks to the maximum quantum efficiency and the capability of optimizing the frequency characteristic by tuning the region responsible for the flight time of carriers, these structures are mainly applied in systems for photomixers, operating in the continuous or quasi-continuous oscillation mode, in which the photocurrent is modulated at the optical beating frequency arising from a superposition of two laser sources [137, 138]. A classical p–i–n photodiode consists of a semiconductor layer with intrinsic conductivity (i), where the absorption of the optical pulse occurs, and the surrounding layers with acceptor (p) and donor (n) types of doping (Fig. 4a). The absorption of photons leads to the formation of electron-hole pairs in the

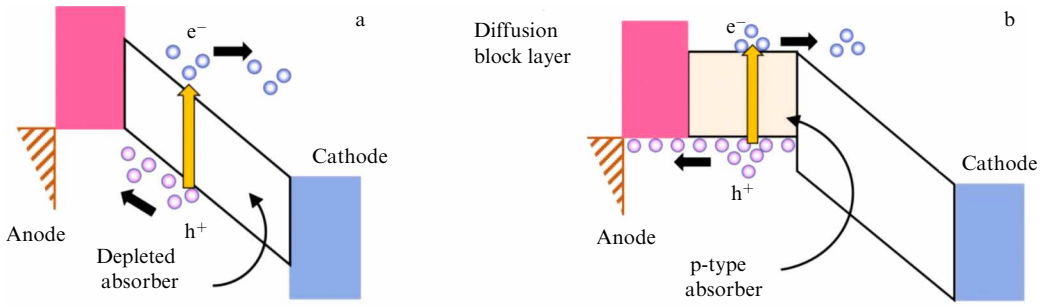


**Figure 4.** Schematic image of the energy band structure and transport of charge carriers in (a) p–i–n photodiode and (b) photodiode with a unidirectional transport of carriers [143].

i layer. Under the action of the built-in field, nonequilibrium electrons and holes drift towards the n and p layers, respectively. Hence, the contribution to the generated photocurrent comes from both the electrons and the holes. While the electrons with a small effective mass can rapidly accelerate, the effective mass of the holes makes them an order of magnitude slower [122].

Although the silicon p–i–n photodiode was studied back in 1991 [139], GaAs-based p–i–n– photodiodes were first used to generate THz radiation in Ref. [140]. In this study, the authors also established the presence of the drift velocity overshoot in photodiodes and the dependence of THz radiation intensity on the magnitude of this overshoot. The flight time of 'heavy' holes from the i layer to the p layer leads to the photocurrent saturation in classical p–i–n photodiode structures and is the main factor limiting the high-frequency part of the spectrum. As an alternative photodiode design, free of such a limitation, a uni-traveling-carrier photodiode model was developed [141, 142], in which the p-doped photoabsorbing layer is located adjacent to a high-bandgap intrinsic layer serving to collect the carriers (Fig. 4b). On the anode side, there is a layer inhibiting diffusion of electrons, due to which a unidirectional motion of electrons towards the collector is formed. Such a construction ensures spatial separation of the absorbing region and the region of carrier acceleration.

Using devices based on the uni-traveling-carrier principle, THz generation powers of $\approx$ 300 and 2.6 μW were reached at 0.3 and 1.04 THz, respectively [144]. The authors of Ref. [145] obtained a record-breaking continuous generation power of $\approx$ 1.04 mW at 0.28 THz.

One more approach to increasing the efficiency is based on using the combined superlattice construction of p–i–n photodiodes, in which several individual diodes are placed one over another [146]. Each individual p–i–n photodiode is optimized to minimize the flight time of photoexcited charge carriers, which is achieved by reducing the i layer thickness to ensure ballistic transport. This significantly decreases the frequency spectrum fall caused by the time of flight. In Ref. [147], based on a superlattice p–i–n photodiode, a generation power of 1 μW at 0.4 THz is demonstrated in the continuous mode.

### 2.3 Using nonlinear media

Depending on the optical scheme, one and the same nonlinear medium can emit or detect freely propagating electromagnetic waves due to optical rectification or linear electrooptical effects, respectively [148, 149]. In terms of transparency and values of the nonlinear susceptibility coefficient, the following structures are suitable for operation in the THz range:

- inorganic crystals $LiNbO_3$ and $LiTaO_3$ [150, 151], enabling significant THz electric field strengths [152];
- semiconductors GaAs [153], GaSe [154], GaP, InAs, InP, and frequently used ZnTe [155];
- organic crystals DAST, DSTMS, OH1, HMQ-TMS, BNA, EPHSI [156, 157];
- $VO_2$ [158] and other films experiencing a metal-to-insulator transition.

In a nonlinear process, a high efficiency of conversion can be achieved if the interaction length of electromagnetic waves is large and the phase matching condition is fulfilled, which happens when the phase velocity of THz wave propagation coincides with the group velocity of the ultrashort laser pulse. The THz and laser pulses become longer in the crystal because of material dispersion, so that the above requirements contradict each other: thinner crystals possess wider ranges of THz generation and spectral sensitivity, but smaller efficiency, and vice versa [155].

### 2.4 Using laser gas discharge plasma

To generate THz radiation and to detect it coherently in the spectral range with a high-frequency boundary of up to 10 THz, the laser gas discharge plasma (filament) arising in the optical breakdown of He, N, air, and other gases can be used [159–161]. THz radiation generation as a result of ponderomotive forces acting in the plasma was first demonstrated by H Hamster [162]. The breakdown was initiated by a single (fundamental) radiation wavelength; therefore, such a regime was called single-color excitation. Later, it appeared possible to increase the efficiency of optical-to-THz conversion due to a transition to the (nonlinear) process of four-wave mixing, in which a two-color laser excitation was used for the gas breakdown simultaneously at the fundamental frequency and the second harmonic frequency [163]. This principle has also been used for the coherent detection of THz radiation in gas-discharge plasma [164].

When generating THz radiation, a laser beam at the fundamental frequency (800 nm) passes through a thin crystal of beta-barium borate ($\beta$-BBO), as a result of which some of the radiation is converted into the second harmonic (400 nm). The gas discharge plasma formation is implemented by using the focused two-color radiation. Detection is a process inverse to two-color excitation, namely, two photons at the fundamental frequency are mixed in the gas discharge plasma with the THz photon, and, in the presence of an external bias electric field, produce one photon of the second harmonic, which is recorded by the photodetector.

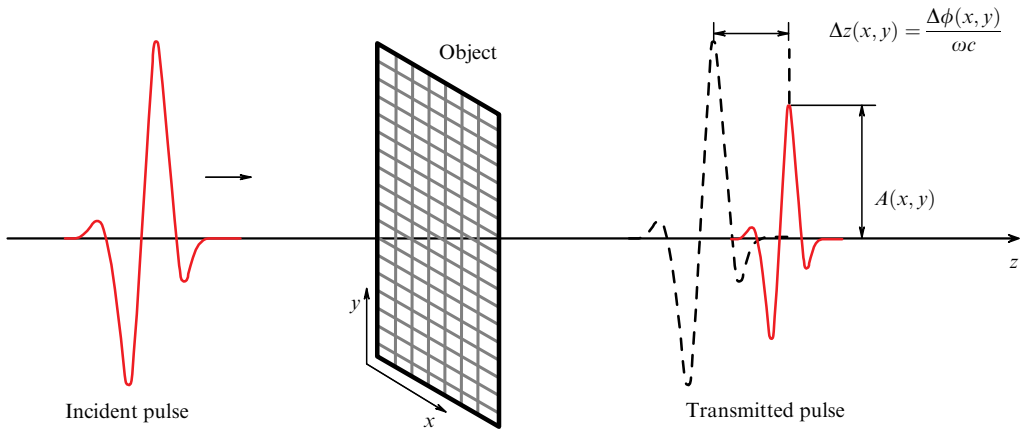


**Figure 5.** Schematic illustration of raster scanning of an object in THz time domain imaging in transmission geometry.

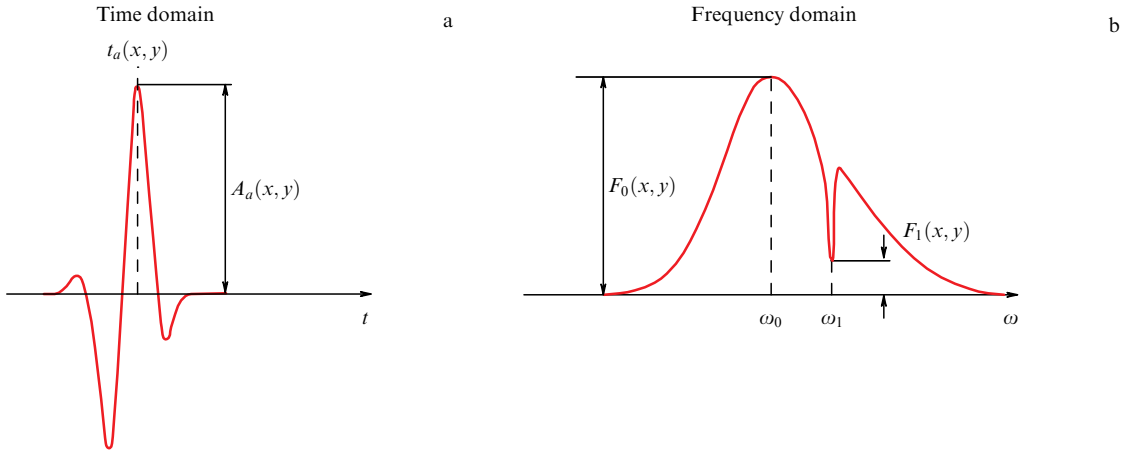


**Figure 6.** Examples of feature choice in THz time-domain imaging aimed at constructing reduced 2D images of an object: (a) maximum amplitude $A_a(x,y)$ and delay time $t_a(x,y)$ of a pulse in the time domain; (b) maximum amplitude $F_0(x,y)$ and amplitude at a specified frequency $F_1(x,y)$ in the frequency domain.

## 3. Time-domain terahertz spectroscopy and imaging

The operation of a THz time-domain spectrometer is based on generating short THz pulses followed by coherent detection of their wave shape. The basic diagram of a THz time-domain spectrometer is presented in Fig. 1. The Fourier transform of the recorded time-dependent signal allows obtaining broadband spectra of a THz wave complex amplitude that carry information on its amplitude and phase. To suppress Gibbs noises in the frequency domain, the apodization procedure, i.e., window filtering in the time domain, is carried out (e.g., using Tukey filters). Hence, the time-domain spectroscopy allows obtaining the most complete information about a THz wave based on a single measurement. This makes possible the fast assessment of the complex amplitude coefficients of absorption and reflection by samples in a wide range of frequencies ($\approx$ 0.1–3.5 THz or wider), as well as solving inverse problems related to reconstruction of the complex permittivity (or optical characteristics) of a sample directly from the spectrometer signals without using the Kramers–Kronig relations.

In turn, the methods of THz time-domain imaging imply raster scanning of the studied object with a focused THz beam (Fig. 5) with subsequent analysis of temporal or spectral (amplitude or phase) information and the distribution of optical or dielectric properties over the object aperture. The image recorded by means of a THz time-domain spectrometer contains much more information than does a usual 2D image with a similar number of pixels. In THz time-domain imaging, each pixel contains a time-dependent spectrometric signal, which opens up wide possibilities for processing and analyzing such data, followed by the construction of reduced parametric images that are convenient for analysis with the naked eye.

Figure 6 illustrates several parameters of time-dependent signals and their Fourier spectra, which can be used to construct THz parametric images of an object. Among them we note the maximum amplitude $A(x,y)$ and the pulse delay time $t_a(x,y)$ in the time domain or the maximum amplitude $F_0(x,y)$ and the amplitude at a given frequency $F_1(x,y)$ in the frequency domain. The last characteristic is particularly useful for THz imaging when the sample under study possesses a characteristic resonant spectral response.

### 3.1 Terahertz imaging using classical optical systems

The principle of THz time-domain imaging was first proposed in Ref. [165], where images of a microchip in a plastic case and a plant lamina were obtained. Due to the capability of THz radiation to penetrate through nonmetallic packing, construction, and building materials, THz time-domain imaging is used for quality inspection, defectoscopy, and detection of hidden forbidden objects and substances [166–168]. In Ref. [169], THz time-domain imaging is applied

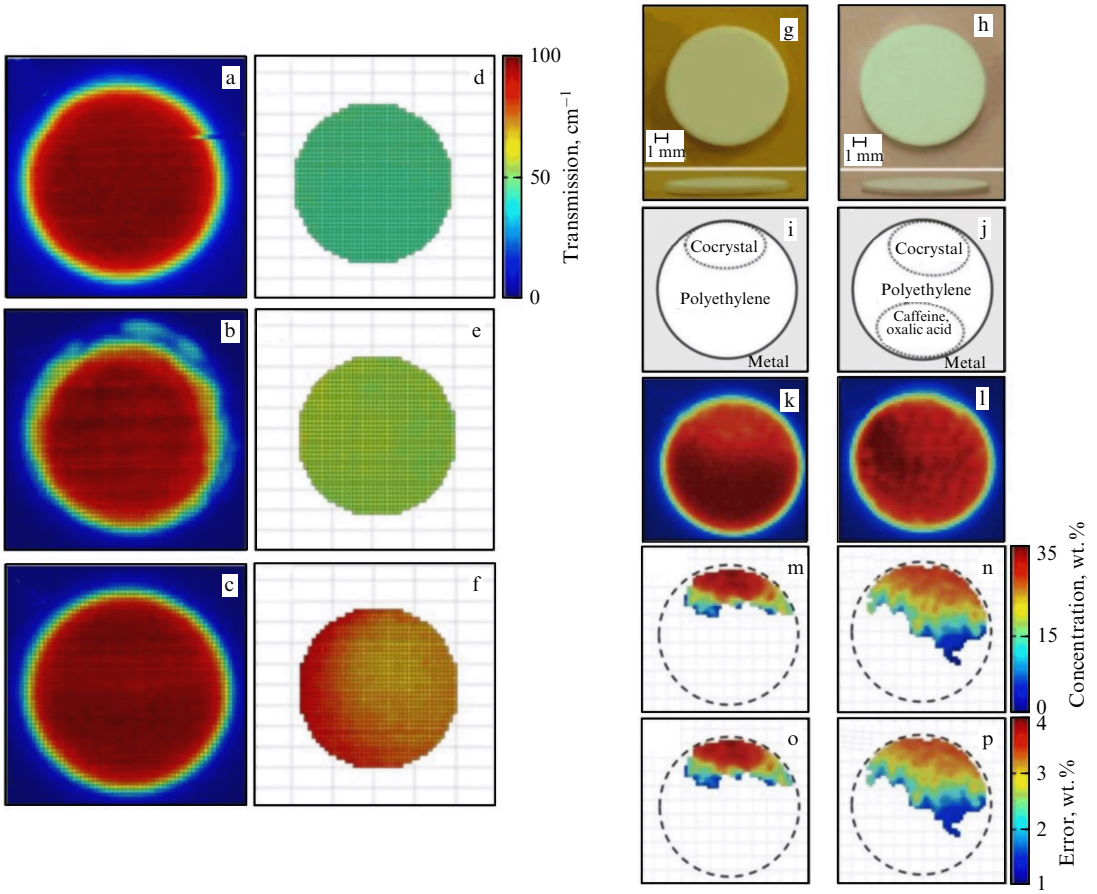


**Figure 7.** Chemical mapping of calibrated (a–f) and nonuniform composition tablets (g–p) [173]: (a–c) chemical mapping of calibrated tablets with a content of 20%, 10%, and 0% of caffeine cocrystal — oxalic acid; (d–f) transmission map at a frequency of 1.56 THz of maximum absorption in the cocrystal, which is absent in absorption spectra of caffeine and oxalic acid separately; (g–p) chemical mapping of cocrystal in a compositionally inhomogeneous tablet: (g, h) optical images; (i, j) composition diagrams of a tablet; (k, l) THz amplitude images; (m, n) cocrystal weight fraction at frequency of 1.56 THz; (o, p) absolute error in the calculated cocrystal concentration.

to water content determination in polyamide and a wooden-plastic composite; the high sensitivity of the THz method is demonstrated by comparing THz data with the results of gravimetric measurements. In Ref. [170], this method was used to detect hidden cavities in cases of integrated circuits to determine their dimensions and thicknesses. In [171], THz time-domain imaging allowed detecting hidden delamination in a glass fiber-based polymer composite material, and, in [172], it enabled detecting defects in welds of similar materials.

The methods of THz spectroscopy and imaging can be used to recognize crystalline solid single phase materials composed of two or more different molecular compounds (cocrystals). In Ref. [173], THz time-domain imaging was used to study cocrystals containing caffeine and oxalic acid, pressed in inhomogeneous tablets (Fig. 7). The method enables determining the mass fraction of a cocrystal in a tablet with an accuracy of 0.3–1.3%. Such investigations were used not only in pharmaceutics to study salicylic acid and sodium salicylate [174] but also in studies of low-temperature spectra of cocrystals of more dangerous compounds, e.g. CL-20/TNT [175].

THz time-domain spectroscopy and imaging open up new possibilities in medical diagnostics, because they are non-invasive and use natural (endogenous) markers to differentiate healthy and pathological tissues [176]. The THz time-domain imaging method has found application in the diagnostics of benign and malignant neoplasms of various nosologies and localization, traumatic damages, burns, scars, tissue viability, hydration, diabetes, and other pathologies [177–179]. Due to the small depth of THz radiation penetration into tissue (it is only $\sim$ 10–100 μm, depending on the electromagnetic wave frequency and tissue type), THz methods allow studying only superficial tissue layers. Correspondingly, they may be applied noninvasively or with minimum invasion to skin and other epithelial tissues, coating the surface and cavities of the human body or intraoperatively for other types of tissues and organs.

Despite the noticeable advantages of time-domain imaging in the THz range, it has a fundamental limitation — the significant time spent on recording a single image, which reaches several minutes or even tens of minutes [180]. Therefore, the search for ways to increase the recording speed of THz images up to a real-time scale has been ongoing since the advent of THz imaging methods. Existing approaches to solving this problem can be conditionally divided into two categories:

- imaging systems based on matrix THz detectors or systems of THz beam sweeps [181, 182], in combination with high-speed detectors;
- imaging systems based on single-pixel detectors and principles of the encoding aperture, excluding raster scanning [183].

Innovative detectors used in the first category of imaging systems include microbolometer [184, 185] or pyroelectric

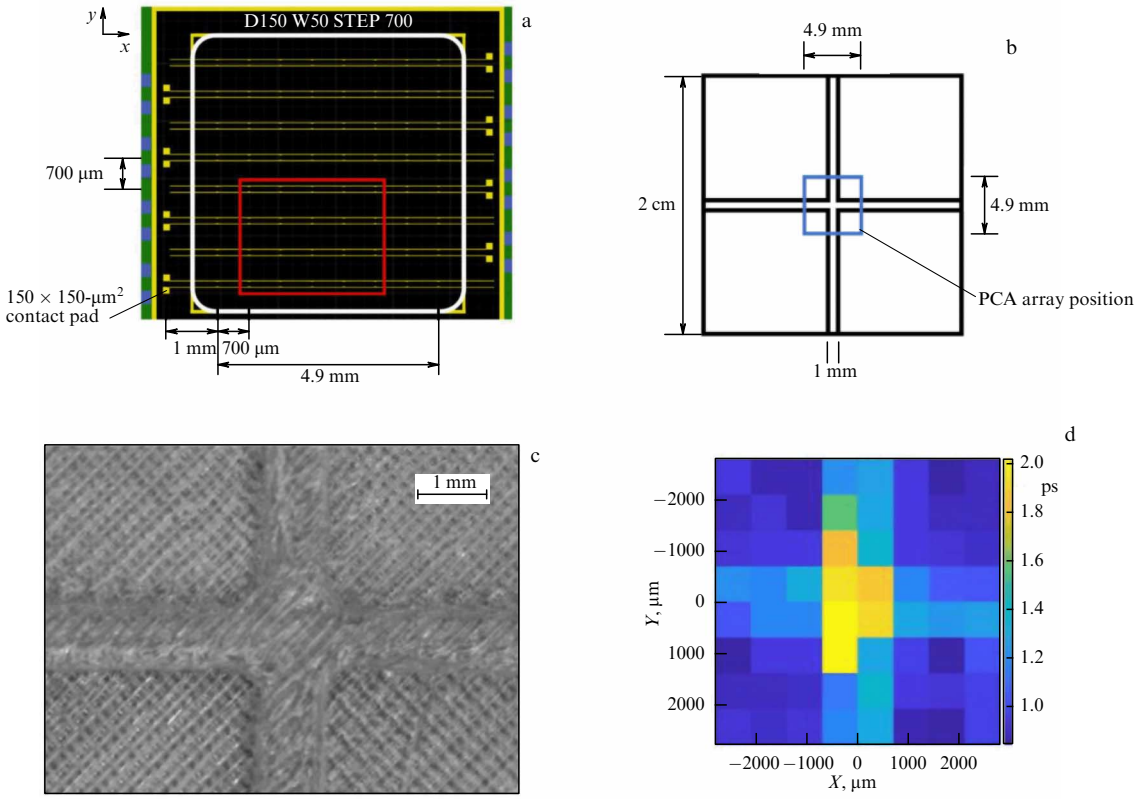


**Figure 8.** Matrix PCA detector for THz imaging [76]: (a) schematic diagram of an 8 × 8-pixel array of antennas; (b) schematic of a polymer test object in the form of a cross on a substrate; (c) test object microscopy; (d) THz image of the test object.

detectors [186], matrices of charge-coupled devices [187], and detectors based on field-effect transistors with high mobility of electrons in the channel [188]. However, in these cases, only the intensity of the THz field is recorded, and the phase information is lost. A promising approach that allows reducing the data acquisition time, saving both the amplitude and the phase information about THz waves, is to use arrays of PCAs. In Ref. [76], a 64-pixel matrix detector (8 × 8 elements) based on a 2D array of PCAs (Fig. 8a) was incorporated in a THz time-domain spectrometer in combination with a spatiotemporal light modulator. In this detector, the electric signal is simultaneously read out from each of 8 pixels in a row, and the light modulator allows probing a particular antenna within this row by means of a femtosecond laser beam. In other words, the pixel row and column in the array of antennas are selected by the electric and optical readout, respectively. In the considered study, a 'phase mask' was considered as one of the objects for THz imaging, which was fabricated by the polymer print method and had the shape of a plastic cross 700 μm thick on a substrate 700 μm thick. Figures 8b, c show a schematic diagram of this mask and the microscopy of its central part, and in Fig. 8d the cross is distinctly seen in the distribution of THz wave amplitude, recorded by the matrix PCA detector. In the current geometry of the matrix PCA detector, the separation between the adjacent elements (pixels) in the array and, correspondingly, the resolution of the THz imaging amounted to 700 μm. An alternative approach to recording the space-time profile of a THz pulse consists in using wide-aperture electrooptical detectors in combination with matrix detectors of the probing laser beam [189–191].

Computational methods of THz imaging based on single-pixel detectors and encoding apertures are attracting more and more interest. In these systems, it is suggested that a set of transparencies transforming the THz wave complex amplitude be introduced successively into the space between the object and a single-pixel detector [192]. The a priori knowledge of the geometry of transparencies allows reconstructing the object image from the observed signals of the detector, the number of transparencies required for this aim being smaller than the number of pixels in the reconstructed image [193, 194]. One of the first papers in the field of THz imaging with encoding aperture is dated 2008 [195], where, for a 32 × 32-pixel image reconstruction, the authors needed only 300 transparencies. In Ref. [196], using this principle, a frame scan rate of 6 Hz was achieved to record 32 × 32-pixel images, i.e., the methods allowed bringing the THz imaging closer to real-time. At the same time, methods of computational THz imaging based on encoding apertures are characterized by specific noises and distortions of images related to solving inverse problems, which limit their practical application.

**3.1.1 Confocal terahertz microscopy.** To enhance the resolution, contrast, and magnification and to increase the signal-to-noise ratio in THz imaging system, the principle of confocal microscopy is also used. First proposed by M Minsky [197] for optical range microscopy, it was later adapted for THz imaging as well. The principle of confocal microscopy consists in using a pinhole diaphragm placed in the plane conjugate to the focal plane of the objective lens. The diaphragm blocks the flow of scattered radiation coming from sample sections other than the focal plane of the objective lens, which improves the contrast and resolution not only in the focal plane, but also over the sample depth. The first experimental study on using a confocal diaphragm in the THz range was carried out by the authors of Ref. [198].

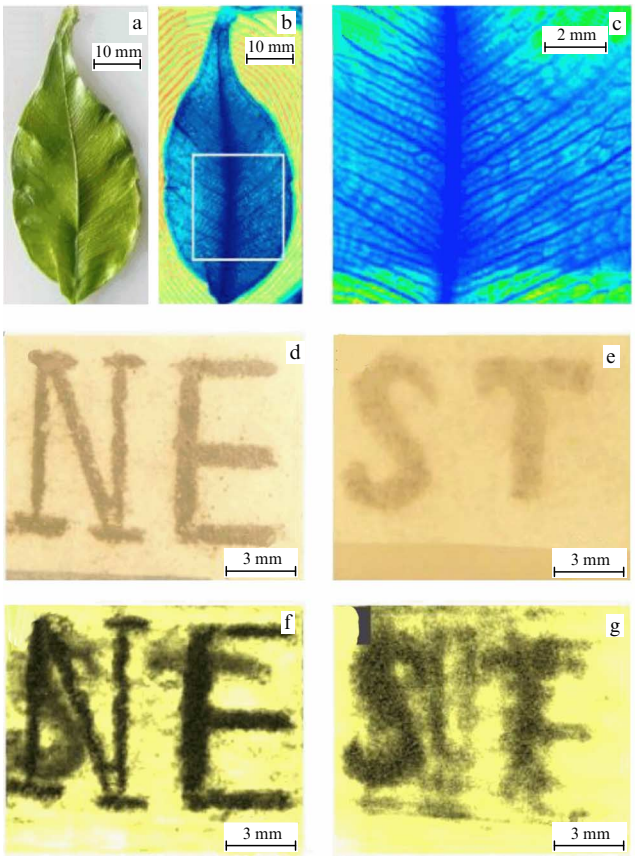


**Figure 9.** Results of studies: (a) optical photograph of a green leaf; (b) high-contrast THz confocal microscopy image of this leaf with distinctly recognizable veins. Recorded with a resolution of $90 \times 160$ pixels; (c) magnified image of the region highlighted with white in Fig. b, recorded with a resolution of $200 \times 200$ pixels; (d, e) optical photographs of two paper sheets with pencil-drawn symbols. For further studies, an object is composed of the sheets, in which (d) is located coaxially above (e) at a distance of 1.2 mm; (f, g) an image of the object, obtained by confocal THz microscopy focusing on the front and back plane, respectively. The resolution of the images is $120 \times 100$ pixels [200].

They used the classical pump–probe scheme of a THz spectrometer based on PCA of semi-insulating GaAs; in this case, a confocal diaphragm was inserted into an intermediate focal plane of the optical system. By analyzing a specially fabricated test sample, making it possible to determine both the spatial resolution and the depth selectivity of THz image, the authors demonstrated that the use of the confocal diaphragm substantially improves the image contrast and ensures a resolution of at least $\lambda/4$.

In subsequent studies, the confocal THz microscopy method was applied using a CW laser. In particular, in [199], an optically pumped $CH_3OH$ gas laser operating at a frequency of 2.52 THz ($\lambda = 118.9$ μm) was used as a source. The lateral resolution in the system amounted to 310 μm, which is 1.5 times better than that of a traditional system with the same optical scheme (for comparison, 460 μm). In addition, the authors estimated the axial (depth) resolution, which amounted to 400 μm. In Ref. [200], a quantum cascade laser generating at a frequency of 2.9 THz was used for the first time as a source of radiation. The lateral and axial resolution was 70 μm and 400 μm, respectively, with a substantial contrast enhancement as compared to the traditional scheme. An example of the image obtained in the confocal microscopy scheme is presented in Fig. 9.

The authors of [201] created a double-axis confocal microscope with an axial resolution of 6770 μm operating at a frequency of 2.52 THz. Due to the crossing of the optical axes, the double-axis scheme provides a better resolution than the single-axis one does, and allows increasing the distance to the object. According to the results of the study, the resolution in the transverse and longitudinal direction amounted to 353 μm and 314 μm, respectively.

It is not only a pinhole that can be used as a confocal diaphragm. In Ref. [202], a system was presented where a focused THz beam is incident on a dielectric cube-like lens. When the radiation passes through this lens, a so-called subwavelength photonic jet is formed at the output [203]. At a characteristic frequency of 0.125 THz, the jet size and the lens output was $0.55\lambda$, whereas in Ref. [204] the result was improved to $(0.39-0.41)\lambda$. Among recent publications, theoretical paper [205] is worth special attention, where a lens-free system of THz imaging based on confocal waveguides was used. Instead of focusing lenses, the authors used hollow waveguides with small losses, comprising a hollow cylindrical polymer carcass, the inner cavity of which was coated with aluminum foil. In addition to the simplicity of manufacturing, the waveguides ensure additional subwavelength focusing with a limit resolution of $0.5\lambda$ and a frequency of 0.1 THz.

### 3.2 Terahertz tomography

As with other methods of tomographic investigations, THz tomography implies the reconstruction of the internal structure of a 3D object. Let us consider two kinds of THz tomography that differ in principle:

- time-of-flight tomography, based on the analysis of echo signals (pulsed responses) due to the reflection of THz pulsed radiation from layered objects;
- computer tomography, based on the analysis of THz radiation transmission measured at different aspect angles using the Radon transform.

**3.2.1 Time-of-flight tomography.** The method of THz time-domain spectroscopy allows direct depth profiling of multilayer structures. When a THz pulse is incident on such a structure, the wave is reflected from the interfaces, so that the resulting reflected signal consists of a series of pulses, corresponding to different interfaces (Fig. 10). The analysis of wave shapes relative to the arrival time with a resolution of $\sim 10-100$ fs allows investigating the sample structure layer-by-layer and estimating the position of interfaces with micron accuracy. Moreover, by analyzing the instantaneous amplitude of the reflected field, it is possible to solve lidar inverse problems and reconstruct refractive index profiles over the depth of the sample [206].

The first studies in the field of THz time-of-flight tomography consisted in the determination of the distance to an object in the THz range [207]. For example, Fig. 11 [208] shows the results of time-of-flight THz tomography of a razor blade lying on a metallic surface in the form of delay maps of the reflected THz pulse and its maximum amplitude for every point of the object. In the left part of the tomographic image, individual reflecting surfaces and characteristic elements of the blade can be distinguished, whereas in the amplitude image (right) no individual surfaces can be distinguished because of close reflection coefficients and the lack of phase information.

In Ref. [209], images of a computer diskette were obtained, in which its constituent parts are distinguishable: the front and back parts of the case, the magnetic disc, and the

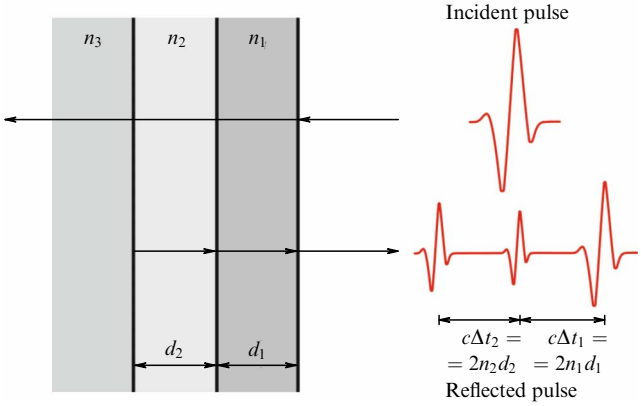


**Figure 10.** Schematic diagram of THz pulse reflection from a multilayer dielectric medium.

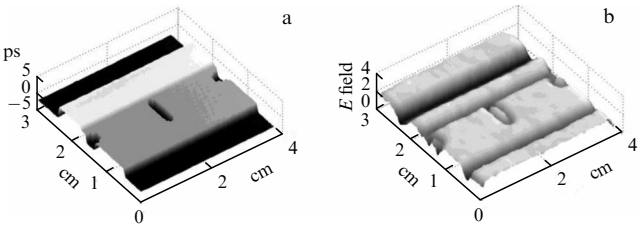


**Figure 11.** THz time-of-flight tomography of a razor blade on a metallic surface [208]: (a) analysis of the arrival time of the reflected THz pulses; (b) analysis of the maximum amplitude of the reflected THz pulses.

metallic bush. In Ref. [210], the method was applied to detect starved-joint defects in the bulk of a polymer composite material and to determine the depth of their deposition.

A promising application of THz time-of-flight tomography is considered in Ref. [211]. The author studied defects in the foam thermal insulation in a space shuttle, which is of fundamental importance for the safety of space flights. Such a medium has a low density and absorption coefficient; it is extremely hard to study using traditional ultrasonic and X-ray methods. In turn, due to its high sensitivity to minor changes in the THz optical properties of the material, time-of-flight tomography allowed determining both the air-filled cavities in its bulk and material delamination in the regions under study. In Ref. [212], using a broadband source of THz pulses based on the 4-dimethylamino-N-methyl-stilbazolium tosylate nonlinear crystal excited by laser pulses with a duration of only 17 fs in combination with the deconvolution of THz pulsed signals, the authors obtained a tomographic image of a multilayer structure with a layer of GaAs only 2 μm thick (Fig. 12).

The authors of Ref. [213] proposed a method of mathematical processing of the signals of time-of-flight THz tomography to analyze optically thin layers, for which the ratio of the layer thickness to the refractive index is less than half of the wavelength. For such a small thickness, the pulses reflected from different layers overlap each other, which makes it impossible to precisely determine the pulse arrival time. To solve this problem, the authors proposed a method of time-dependent signal deconvolution using autoregression spectral extrapolation based on the modified covariance method. The method allows achieving even greater resolution in the analysis of fine multilayer structures.

**3.2.2 Computer tomography.** Computer tomography in the THz range, in general, uses the same principles as X-ray tomography, namely, a series of 2D shadow (transition geometry) images of an object rotating about its axis is recorded. Then, using the Radon transform [214, 215], the inverse problem of computer tomography is solved and a 3D image is reconstructed, reflecting the distribution of the local coefficient of THz absorption. It is important to note that, in contrast to the X-ray range, the refractive indices of the objects of study substantially differ from that of the free space ($n > 1.0$), which gives rise to a refraction of the THz radiation at the interfaces. It is extremely hard to take this effect into account when solving the inverse problem of computer tomography, which leads to a distortion of the resulting THz thermograms, while substantially restricting the scope of media to be studied by this method. Moreover, this method is inapplicable to opaque (strongly absorbing) dielectric media in the THz range, including biological tissues and other water-containing objects.

THz computer tomography was first implemented in Ref. [216], where the authors used a piece of turkey bone *ex vivo* as the object of study. The transmission of broadband THz pulsed radiation through the sample was recorded at different aspect angles, and the inverse projection algorithm with filtering, for which the amplitudes of THz pulses served as the input data, was used to reconstruct the THz tomogram. Figure 13 shows the experimental system and an example of 3D image reconstruction. Forming such a THz tomogram required raster scanning of the object with a beam ($100 \times 100$ points) from multiple aspect angles.

In Ref. [217], test objects in the form of a polystyrene vessel with various materials inside it (metal, Teflon, glucose, and lactose) were studied by means of THz computer tomography. Using a focused beam of THz pulsed radia-

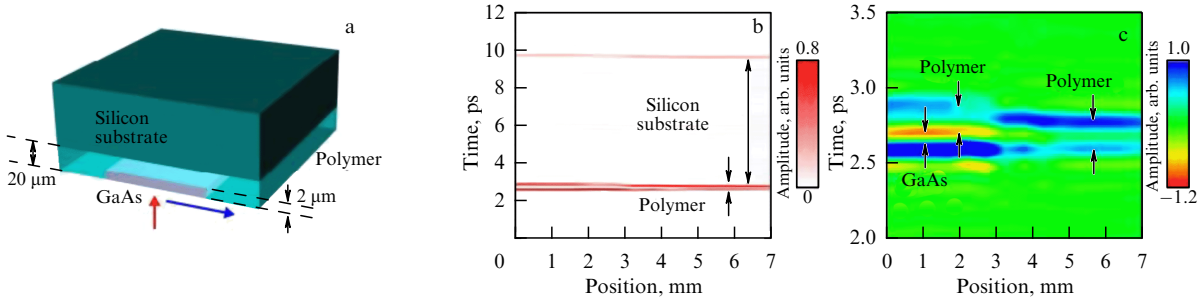


**Figure 12.** THz time-of-flight tomography of a semiconductor structure with a GaAs layer 2 μm thick [212]: (a) schematic of the semiconductor structure; (b, c) THz image and its magnified region with the GaAs layer.

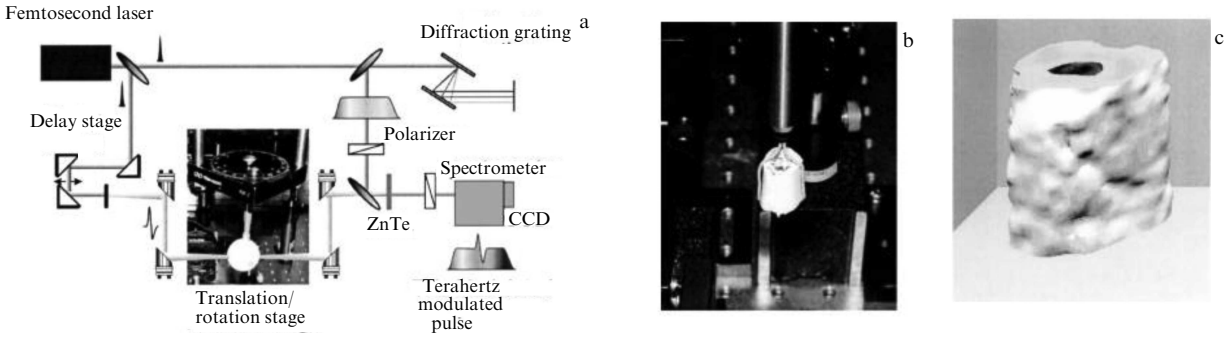


**Figure 13.** THz computer tomography of a turkey bone *ex vivo* [216]: (a) schematic diagram of the experimental setup based on a THz time-domain spectrometer; (b) sample photograph; (c) THz tomogram.

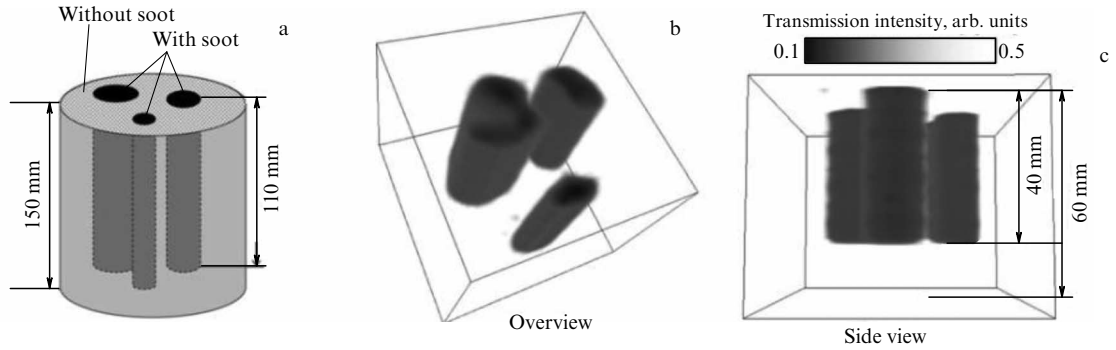


**Figure 14.** THz computer tomography of soot filters for combustion engines [218]: (a) schematic diagram of a soot filter with three cavities filled with soot; (b, c) THz tomograms of the filter.

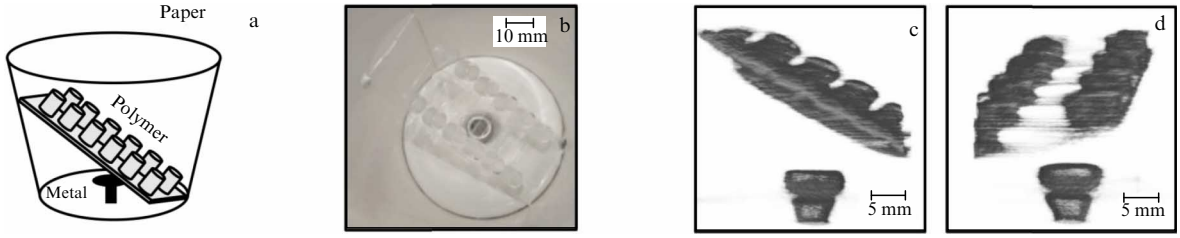


**Figure 15.** THz computer tomography completed with neural network techniques [220]: (a) schematic diagram and (b) photograph of a test object, composed of a paper vessel, polymer block, and metallic screw; (c, d) THz tomograms of the test object.

tion, the inner structure of the vessel was studied with a resolution up to 0.4 mm. Moreover, the THz computer tomography allowed differentiating materials by the character of the reconstructed spectra of their absorption.

In Ref. [218], THz computer tomography was applied to nondestructive control of soot filters for combustion engines having a cellular ceramic structure. First, the THz spectral characteristics of a clean filter and the soot were studied, after which a method of assessing the amount of soot in a dirty filter was developed based on the THz spectra. Then, the dependences of THz radiation transmission through the filters on the frequency and the incidence angle were recorded. Using a Gunn diode as a source of radiation at 65 GHz, three-dimensional images of the filter were obtained by means of THz computer tomography with clearly-seen cavities filled with soot (Fig. 14).

In Ref. [219], the speed of THz computer tomography was significantly increased by using a high-power source of THz pulses based on an $LiNbO_3$ crystal (electric field strength up to 7 kV $cm^{-1}$). The total time of recording THz images for tomographic reconstruction was 6 min.

To increase the efficiency of THz computer tomography methods, the processing of THz images and the solution to the inverse problem were completed with neural network methods [220, 221]. A neural network allows processing THz images (projections) represented in both space-time and space-frequency domains, after which the Radon transform is applied to reconstruct the THz tomogram. Figure 15 shows an example of recording a THz tomogram by a system completed with a neural network.

Reference [222] is devoted to the study of internal defects of high-voltage cables by means of THz computer tomography. In this paper, a frequency-modulated imaging system with a continuous-wave radiation source is used. Linear scanning with axial rotation makes it possible to acquire a three-dimensional data array and to construct a three-dimensional cable image. The image enables distinct characterization of air- and water-filled cavities in the polyethylene insulation, as well as an assessment of twisting a multicore cable inside and the ruptures of individual cores.

### 3.3 Near-field terahertz scanning microscopy

All the THz imaging techniques described above operate in the far field mode and exploit diffraction-limited lens or mirror optical systems; therefore, their space resolution is restricted by the Abbe diffraction limit ($\approx 0.5\lambda$ upon focusing in the free space). It is possible to overcome this fundamental physical limit by means of various methods of scanning probe near-field optical microscopy.

The first experimental studies in the field of THz scanning probe near-field microscopy were carried out back in the 1990s [223, 224]. Since that time, various designs of such systems have been proposed based on various types of near-field probes: subwavelength apertures [225–228], cantilevers (metal needles) [229–231], electrooptical probes [232, 233], or miniature photoconductive THz detectors [234, 235].

**3.3.1 Systems based on subwavelength apertures.** In pilot studies on THz near-field microscopy, a subwavelength aperture [223] was used to restrict the THz spot size, by analogy with the known methods used in the visible [236, 237] and IR [238] ranges. In this case, the aperture was a sharpened metal conical tip with a subwavelength hole at the narrow end, the resolution in the recorded image being determined by the hole size. Although a smaller aperture diameter $d$ provides a higher resolution, the energy characteristics of such a microscope (e.g., signal-to-noise ratio in the recorded images) sharply fall with a decrease in $d$ [239–241].

Various geometries of the subwavelength aperture have been investigated. In Ref. [242], the authors proposed using as the near-field dynamic aperture a laser beam focused on the studied sample to provide a local change in its conductivity, the space resolution of the methods being determined by the sharpness of the laser beam focusing. When studying a metallic drawing on a GaAs substrate, a resolution of $< 50$ μm was achieved. In [243], a resolution of up to $\sim \lambda/100$ was obtained at a frequency of 1 THz, the aperture size being 3 μm. The aperture diameter determines the frequency of radiation that can be passed through it. The minimum frequency of possible transmission is called the cutoff frequency $v_0$, below which a substantial decay of the signal occurs [244]. A few approaches are being developed that ensure the possibility of working at frequencies below $v_0$. The authors of Ref. [245] used a plasmonic waveguide based on two metallic plates to enable a resolution up to $\lambda/250$. In Ref. [246], a double-needle probe was proposed, which, due to surface plasmon modes, provides a resolution of THz imaging to 10 μm. In Ref. [247], an aperture with increased transmission at frequencies below $v_0$ is proposed. The authors of [248] created a truncated cone-shaped aperture probe of plastic, providing a resolution up to 6 μm at 0.11 THz, or $\lambda/450$.

A subwavelength aperture can be used together with a subwavelength THz detector. In Refs [226, 241], the aperture was fabricated and localized in the immediate vicinity of the PCA detecting region. In this case, the PCA is more sensitive to the weak field of evanescent waves passing through the aperture. For object raster scanning with such an aperture, the resolution achieved 7 μm at 0.2 THz, or $\lambda/200$. In Ref. [249], a near-field aperture was also combined with a PCA detector, the antenna comprising an $AlAs/Al_{0.2}Ga_{0.8}As$ Bragg reflector under an LT-GaAs photoconductive layer and an array of gold nanoantennas on the photoconductor surface. This structure allowed demonstrating a subwavelength resolution up to 2 μm at 1 THz, or $\lambda/150$.

The idea of integrating a near-field probe with a detector was developed in Ref. [250]. For detection, a thermoelectric mechanism was used in the channel of a field-effect transistor, consisting of asymmetric electrodes and an InAs nanostring channel between them. This idea was tried for THz imaging in Ref. [228], where a system of supersensitive subwavelength imaging has been manufactured, including the above detector, an aperture 18 μm in diameter, and an interferometer optical system based on a THz quantum cascade laser. The achieved minimum detected power amounted to 7.6 nW.

**3.3.2 Aperture-free near-field terahertz microscopy.** The method of scanning probe near-field optical microscopy developed in the 1990s and based on a subwavelength scattering cantilever [251, 252] was translated to the THz range in the 2000s [253, 254]. The cantilever (a sharpened metallic probe) was kept near the sample surface at a distance of the order of the probe tip curvature radius [230, 231] and was illuminated with a focused THz beam. The conditions for THz field scattering at the cantilever tip depend on its closeness to the object and on local optical and structural properties of the object. The field scattered by the cantilever is detected in the immediate vicinity of it [253] or in the far-field zone. To increase the signal-to-noise ratio in the recorded signals, the probe oscillates in the direction normal to the object surface at a low frequency ($\sim 100$ Hz) at which THz signal demodulation is then performed using the synchronous detector principle.

To physically interpret the data of this kind of THz microscopy, a model where the 'cantilever–object surface' system forms a Mie scatterer was proposed [255, 256]. Within the framework of the Mie theory, the probe is considered a simple spherical scatterer placed above the plane surface. This approach was first used by the authors of Ref. [257], who based it on the quasiclassical theory to describe the interaction between a polarized sphere approximating the probe and its image in the sample, induced by surface charges. Although this model provides adequate interpretations of near-field microscopy in the visible and IR ranges, the authors of [255] note that it does not agree with the data they have obtained. To explain this fact, a model is proposed in which the probe tip is not considered to be a Mie scatterer, but a dipole antenna resistively and inductively coupled to the incident THz radiation. A similar model is used in Ref. [258] to explain the relatively weak decay of the near field amplitude upon increasing the gap between the tip and the surface. A comparison of different models is carried out by the authors of Ref. [259]. K Moon et al. [260, 261] proposed a new analytical theory, which is in perfect agreement with the experimental results. In this theory, the probe is approximated not simply as an individual point dipole but as a continuous distribution of dipoles over its volume, which commonly is replaced by a point dipole for simplicity. V N Trukhin et al. [262] studied the processes of scattering of pulsed THz radiation by metallic probes of a near-field microscope, including those occurring under an increase in the modulation amplitude in the vertical direction of the probe. They showed that, in the process of scattering of a plane electromagnetic wave by a metallic probe, the excitation of diffraction edge waves at the light-shadow interface plays an important role. Since, upon an increase in the probe oscillation amplitude, the signal at the modulation frequency can become comparable to the THz near-field signal [263], to study the effect of interaction of the near-field component of

the electric field with the object near the probe, it is necessary to modulate the oscillation amplitude of the probe so that the phase modulation contribution to the registration of the THz near-field signal is a minimum. It is important that the spatial resolution of THz scanning probe near-field microscopy based on a metal cantilever be determined by the sphericity radius of the probe tip and its separation from the sample surface. The values of both can be much less than the THz wavelength, and the THz imaging resolution can reach $10^{-3}-10^{-4}\lambda$.

Direct detection of the THz field scattered by a cantilever was used in Ref. [253], where an electrooptical $\langle 100\rangle$-oriented GaP crystal with a sample placed on it was used as a detector. At the expense of scattering in all directions, the immobile probe tip creates a field with components of all polarizations. The choice of such a crystal allows making the system insensitive to the incident THz field and detecting only the near-field components oriented perpendicular to the crystal surface. The resolution of this system reached $\sim 8$ μm when operating in the frequency band of 0.1–1.5 THz. Although direct detection due to the closeness of the detector to the probe provides a high signal-to-noise ratio, this method did not become widespread.

Based on the scheme with an oscillating probe, various studies have recently been carried out. Reference [264] investigated the effects of the near-field interaction of THz radiation with graphene ribbons near a metallic probe of an atomic force microscope. In Refs [265, 266], using THz near-field microscopy, subwavelength metallic nanostructures were investigated in the frequency range from GHz to THz, as a result of which it was discovered that, in this range, the near-field contrast of the studied object extremely highly depends on the transverse dimension of the nanostructure, in contrast to the spatial resolution. The observed contrast also depends on the connection of the nanostructures to the massive ground bus. The results obtained can be explained using quasi-electrostatic analysis, taking into account the size and geometry of metal nanostructures.

In Ref. [267], a THz near-field microscope was developed based on a detector-free laser interferometer system with feedback, in which a semiconductor laser was used simultaneously as a source and as a phase-sensitive detector. This scheme is remarkable for its high compactness, and its implementation allows extending the area of THz microscopy application. It was established that the best result from the point of view of signal-to-noise ratio is ensured in the strong feedback mode, in which the THz microscopic image of a particle of the topological insulator $Bi_2Te_{2.2}Se_{0.8}$ only 39 nm in size (diameter), having active phonon modes in the range of 1.6–2.8 THz, was obtained [268].

To date, imaging individual small biological objects, such as protein molecules, has been a nontrivial problem, also due to the weakness of THz waves backscattered by them. In Ref. [269], this problem was solved using a graphene substrate with a high reflection coefficient, on which the molecule was placed, and a high-efficiency platinum near-field probe. In this way, a topographic and THz near-field image of a single molecule of immunoglobulin G and a molecule of ferritin a few nanometers in size were obtained.

The authors of Ref. [270] proposed a setup with a THz near-field microscope, in which a quantum cascade laser at 4.2 THz as a source and a quantum well photodetector with resonance absorption at the source frequency are used. The high speed of this detector is important with regard to the high modulation rate of the THz beam power flux by the oscillating probe. By means of this THz microscope, images of nanostructures are obtained with a spatial resolution of 95 nm, or $\approx \lambda/752$. In Ref. [271], the possibility of using THz near-field microscopy for studying photonic modes in microcavities was studied. Near-field images were obtained of the electric field distribution in the arms of the logarithmic spiral PCA (Fig. 16d) in the mode of photoexcitation at a frequency of 2.5 THz. The results turned out to be unexpected because of the asymmetry in the field distribution, which was not observed in the calculated distribution (Fig. 16c). The authors concluded that the interpretation of THz microscopic images of the local electric field is nontrivial and the result of imaging strongly depends on the probe position.

Unique for near-field THz imaging are the studies by R Stantchev et al. applying the well-studied classical far-field imaging method of a single-pixel detector [272] and further development of these studies with the implementation of the compressed sensing algorithm [273]. In [272], the authors projected a time-dependent optical pattern of high intensity ($> 100$ μJ cm$^{-2}$) on a silicon substrate 115 μm thick, which spatially modulated the transmitted THz pulsed radiation. The object of study was placed at the back side of the substrate and the single-element detector fixed the transmitted THz pulse in the far-field zone, depending on the encoding mask formed in the object plane. Images of a printed circuit board were obtained with a subwavelength resolution of $\approx 100$ μm at 0.75 THz, or $\approx \lambda/4$. In Ref. [273], a similar system of measurements was used, except the thickness of the silicon substrate was 6 μm. The ultra-thin substrate allowed achieving a resolution of $\approx 9$ μm at 0.75 THz, or $\approx \lambda/45$.

**3.3.3 Solid immersion microscopy.** Another method of near-field imaging is microscopy based on the solid immersion effect. This approach was first proposed in 1990 for optical schemes in the visible and near IR ranges [274, 275] and was recently implemented in systems in the THz range [276, 277]. The solid immersion effect makes it possible to enhance the spatial resolution of an optical system by focusing a beam of electromagnetic radiation at a small distance ($\sim \lambda$) behind an immersion lens with a high refractive index [278]. The immersion lens, as a rule, is made in the form of a truncated sphere and is placed so that the converging beam is incident concentrically relative to the spherical surface [279]. Hence, no refraction of the rays occurs in the immersion lens, and the enhancement of the spatial resolution is achieved by focusing the beam in the near–field zone on the back side of the lens. Due to the high refractive index $n_{SI}$ of the lens, the high-aperture part of the beam experiences total internal reflection (TIR) ($\theta_{TIR} \leqslant \theta \leqslant \theta_{max}$, where $\theta_{TIR}$ is the TIR critical angle, $\theta_{max}$ is the aperture angle) at the immersion lens–object interface, which is accompanied by the excitation of evanescent waves, which interfere with the low-aperture part of the beam ($\theta < \theta_{TIR}$) experiencing a usual Fresnel reflection and form the resulting caustic of the optical system (Fig. 17a). The advantage of this approach over methods of scanning probe microscopy is the high energy efficiency due to the absence of subwavelength diaphragms and cantilevers, whereas the spatial resolution of a THz microscope based on the solid immersion effect may reach $0.15\lambda$ [276, 280], which is comparable to some systems of scanning probe microscopy. As a rule, this method is applied in combination with point-by-point scanning of the object's surface [276, 278]; however,

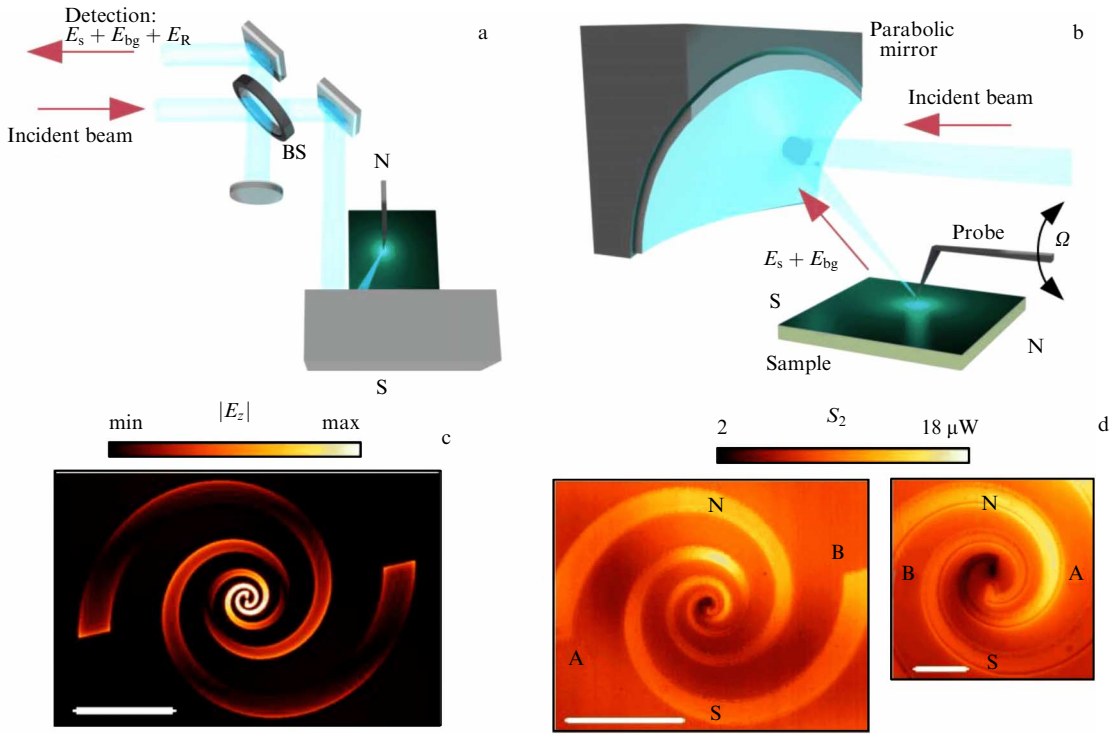


**Figure 16.** THz near-field microscopy of the electric field in the arms of a logarithmic spiral PCA [271]. (a) Schematic diagram of a THz microscope where the beam from a methanol gas laser pumped by a $CO_2$ laser at a frequency of 2.522 THz passes through a microscope interferometer and is focused by a parabolic mirror on the oscillating tip of the probe. Parabolic mirror also collects the scattered radiation in the near field. Optical signals are joined with the reference arm of the interferometer and detected with an InSb hot-electron bolometer. (b) Side view of the parabolic mirror, probe, and sample. (c) Calculated near-field image of electric field intensity ($|E_z|^2$) distribution for a PCA with logarithmic spiral topology in the detector mode. Scale bar is 30 μm. (d) Experimental image of the electric field distribution for a PCA with logarithmic spiral topology in the detector mode: on the left — full-scale with scale bar length of 30 μm, on the right — magnified central part of the PCA with scale bar length of 5 μm is shown.

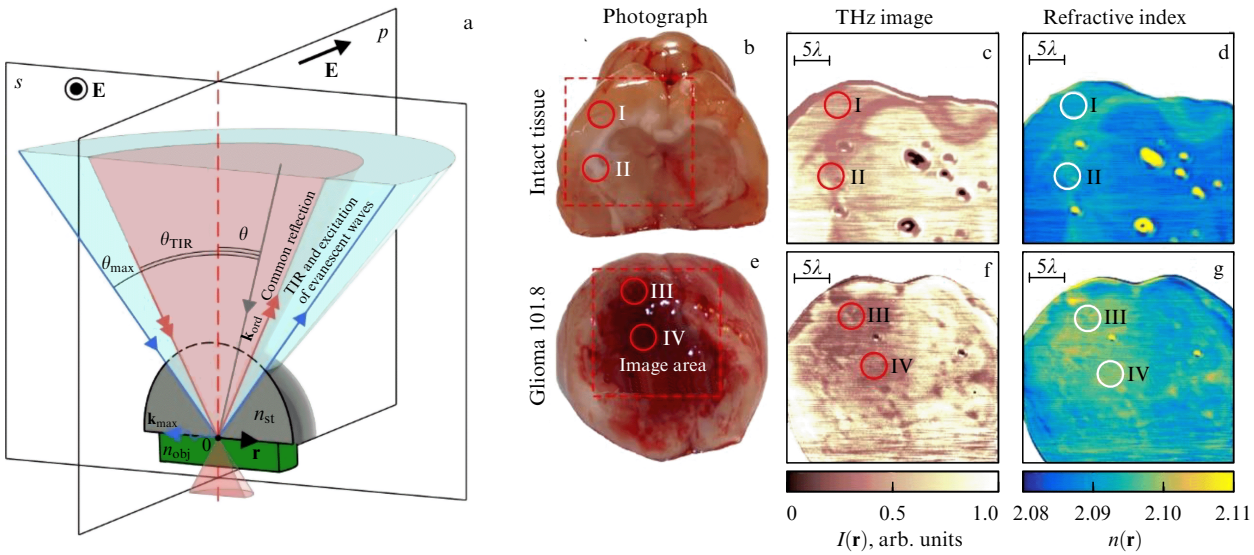


**Figure 17.** (a) Schematic diagram of focusing a THz beam in an optical system based on the solid immersion effect [279]; (b–d) photograph, THz image and the distribution of the refractive index of intact tissue of the rat brain *ex vivo*, obtained using a THz microscope based on the solid immersion effect; (e–g) similar images for the glioma model 101.8 in the rat brain [285].

systems have also been proposed recording THz images in a large field of view [281].

Earlier, the prospect of applying THz microscopy based on the solid immersion effect for nondestructive testing [280] as well as in biomedicine [278, 282] was shown. The results of THz imaging of various types of biological objects and tissues allowed distinguishing their subwavelength features and structures. In particular, this method made it possible to obtain THz images of fat cells and their agglomerations in the connective fibrous tissue of mammary glands [278], as well as intact rat brains and the glioma model 101.8 (Fig. 17c, f) [283, 284]. In addition, a method of analyzing images of THz microscopy based on the effect of solid immersion was proposed, which allowed assessing the distribution of the

refractive index in the object based on the recorded intensity of CW THz radiation [285]. Figures 17d, g show an example of the assessment of the refractive index distribution in the intact brain and glioma 101.8 in the rat brain *ex vivo* using the data of THz microscopy based on the effect of solid immersion at a wavelength of $\lambda = 500$ μm.

Since the resolution of an optical system based on the effect of solid immersion depends on the refractive index of the immersion lens [286], the use of new materials for its manufacturing is a promising way of developing this method. For example, in Ref. [278], a composite material produced by sintering powders of polypropylene and titanium dioxide ($TiO_2$) was used to produce an immersion lens, which allowed reaching a resolution of $0.2\lambda$. The use of composite materials makes it possible to control the optical properties of the immersion lens and, therefore, to change the characteristics of the system.

## 4. Conclusion

The paper presents a review of multispectral imaging results, which became possible due to progress in the up-to-date optoelectronic component base and, particularly, optical-to-THz switches and systems of time-domain THz spectroscopy based on them. The considered switches are based on the following physical principles: charge carrier acceleration in semiconductors when using photoconductive antennas and methods of increasing their efficiency, as well as the generation of THz radiation in p–i–n diodes with the use of nonlinear media of gas discharge plasma.

The most relevant methods of imaging in the THz range are analyzed and the results of studies are presented. For THz imaging methods based on classical optical schemes with diffraction-limited resolution, along with topical results, approaches to reducing the imaging time at the expense of single-pixel detection or compressed sensing are considered. The results of applying the confocal microscopy approach to the THz range are presented. In the section devoted to reconstructing 3D images in the THz range, tomographic imaging methods are described. They include time-of-flight tomography that enables profiling the depth of multilayer structures and computer tomography based on the well-known Radon transform adapted to time-domain THz spectroscopy. The principle of operation is presented and the existing problems and results of imaging by means of near-field THz scanning probe microscopy (beyond the Abbe diffraction limit) based on subwavelength apertures and also more advanced aperture-free near-field microscopy are discussed. Microscopy methods based on the solid immersion effect are considered.

**Acknowledgments.** The works was carried out under financial support from the Ministry of Science and Higher Education of the Russian Federation, project no. 075-15-2020-790.

## References

1. Yu C et al. *Quant. Imaging Med. Surg.* **2** (1) 33 (2012) https://doi.org/10.3978/j.issn.2223-4292.2012.01.04
2. Globisch B et al. *J. Appl. Phys.* **121** 053102 (2017)
3. Kohlhaas R B et al. *Appl. Phys. Lett.* **114** 221103 (2019)
4. Yachmenev A E et al. *Prog. Cryst. Growth Charact. Mater.* **66** 100485 (2020)
5. Singh A et al. *Light Sci. Appl.* **9** 30 (2020)
6. Kohlhaas R B et al. *Appl. Phys. Lett.* **117** 131105 (2020)
7. Yang S-H et al. *IEEE Trans. Terahertz Sci. Technol.* **4** 575 (2014)
8. Carr G L et al. *Nature* **420** 153 (2002)
9. Gorshunov B et al. *Int. J. Infrared Millim. Waves* **26** 1217 (2005)
10. Booske J H et al. *IEEE Trans. Terahertz Sci. Technol.* **1** 54 (2011)
11. Ramian G *Nucl. Instrum. Meth. Phys. Res. A* **318** 225 (1992)
12. Eisele H *Electron. Lett.* **46** 422 (2010)
13. Asada M, Suzuki S *Sensors* **21** 1384 (2021)
14. Williams B S *Nat. Photon.* **1** 517 (2007)
15. Khalatpour A et al. *Nat. Photon.* **15** 16 (2021)
16. Martin Y C, Wickramasinghe H K *J. Appl. Phys.* **91** 3363 (2002)
17. Lee Y-S *Principles of Terahertz Science and Technology* (New York: Springer, 2009)
18. Kafka J D, Watts M L, Pieterse J-W J *IEEE J. Quantum Electron.* **28** 2151 (1992)
19. Auston D H *Appl. Phys. Lett.* **26** 101 (1975)
20. Auston D H, Smith P R *Appl. Phys. Lett.* **43** 631 (1983)
21. Klochkov A N et al. *Opt. Spectrosc.* **128** 1010 (2020); *Opt. Spektrosk.* **128** 1004 (2020)
22. Krotkus A *J. Phys. D* **43** 273001 (2010)
23. Malevich V L *Semiconductors* **40** 155 (2006); *Fiz. Tekh. Poluprovodn.* **40** (2)160 (2006)
24. Tani M et al. *Appl. Opt.* **36** 7853 (1997)
25. Tani M et al. *Meas. Sci. Technol.* **13** 1739 (2002)
26. Look D C *Thin Solid Films* **231** 61 (1993)
27. Lewis R A *J. Phys. D* **52** 433001 (2019)
28. Gupta S et al. *Appl. Phys. Lett.* **59** 3276 (1991)
29. Zamdmer N et al. *Appl. Phys. Lett.* **75** 2313 (1999)
30. Liu T-A, Tani M, Pan C-L *J. Appl. Phys.* **93** 2996 (2003)
31. Mangeney J *J. Infrared Millim. Terahertz Waves* **33** 455 (2012)
32. Johnson M B, McGill T C, Paulter N G *Appl. Phys. Lett.* **54** 2424 (1989)
33. Castro-Camus E et al. *Opt. Express* **15** 7047 (2007)
34. Arlauskas A et al. *Appl. Phys. Express* **5** 022601 (2012)
35. Yachmenev A E, Khabibullin R A, Ponomarev D S *J. Phys. D* **55** 193001 (2022)
36. Glinskiy I A et al. *Nanotechnol. Russia* **17** (Suppl. 1) S24 (2022)
37. Sethi S, Bhattacharya P K *J. Electron. Mater.* **25** 467 (1996)
38. Fernandez Olvera A D J et al. *Opt. Express* **25** 29492 (2017)
39. Nandi U et al. *Opt. Lett.* **45** 2812 (2020)
40. Gorodetsky A, Bazieva N, Rafailov E U *J. Appl. Phys.* **125** 151606 (2019)
41. Gorodetsky A et al. *IEEE J. Sel. Top. Quantum Electron.* **29** 8500505 (2023)
42. Kruczek T et al. *Appl. Phys. Lett.* **101** 081114 (2012)
43. Leyman R R et al. *Laser Photon. Rev.* **10** 772 (2016)
44. Yadav A et al., in *2022 Intern. Conf. Laser Optics, ICLO 2022, St. Petersburg, Russian Federation, 20–24 June 2022, Proc.* (St. Petersburg: IEEE, 2022) https://doi.org/10.1109/ICLO54117.2022.9840021
45. Gorodetsky A, Leite I T, Rafailov E U *Appl. Phys. Lett.* **119** 111102 (2021)
46. Takazato A et al. *Appl. Phys. Lett.* **90** 101119 (2007)
47. Suzuki M, Tonouchi M *Appl. Phys. Lett.* **86** 051104 (2005)
48. Chimot N et al. *Appl. Phys. Lett.* **89** 083519 (2006)
49. Chen Y et al. *Appl. Phys. Lett.* **72** 439 (1998)
50. Kohlhaas R B et al. *Opt. Lett.* **43** 5423 (2018)
51. Dietz R J B et al. *Opt. Express* **19** 25911 (2011)
52. Dietz R J B et al. *Appl. Phys. Lett.* **103** 061103 (2013)
53. Ponomarev D S et al. *J. Appl. Phys.* **125** 151605 (2019)
54. Richter P-H et al. *IEEE Trans. Terahertz Sci. Technol.* **10** 167 (2020)
55. Näser A et al. *Appl. Phys. Lett.* **67** 479 (1995)
56. Kohlhaas R B et al. *Appl. Phys. Lett.* **112** 102101 (2018)
57. Kuznetsov K A et al. *Nanomaterials* **12** 3779 (2022)
58. Siebert K J et al. *Jpn. J. Appl. Phys.* **43** 1038 (2004)
59. Loata G C et al. *Appl. Phys. Lett.* **91** 232506 (2007)
60. Loata G C et al. *Appl. Phys. Lett.* **90** 052101 (2007)
61. Budiarto E et al. *IEEE J. Quantum Electron.* **32** 1839 (1996)
62. Rodriguez G, Taylor A J *Opt. Lett.* **21** 1046 (1996)
63. Yoneda H et al. *Appl. Opt.* **40** 6733 (2001)
64. Xu M et al. *Appl. Phys. Lett.* **103** 251114 (2013)
65. Yardimci N T, Lu H, Jarrahi M *Appl. Phys. Lett.* **109** 191103 (2016)
66. Yardimci N T, Jarrahi M *Sci. Rep.* **7** 42667 (2017)
67. Yardimci N T et al. *Appl. Phys. Lett.* **113** 251102 (2018)

68. Burford N M, El-Shenawee M O *Opt. Eng.* **56** 010901 (2017)
69. Lavrukhin D V et al. *Semicond. Sci. Technol.* **34** 034005 (2019)
70. Chernomyrdin N V et al. *J. Appl. Phys.* **131** 123103 (2022)
71. Park S-G, Melloch M R, Weiner A M *IEEE J. Quantum Electron.* **35** 810 (1999)
72. Lavrukhin D V et al. *IEEE Trans. Terahertz Sci. Technol.* **11** 417 (2021)
73. Ponomarev D et al., in *2022 IEEE Photonics Society Summer Topicals Meeting Series, Cabo San Lucas, Mexico, 11–13 July 2022* (Piscataway, NJ: IEEE, 2022) p. 1, https://doi.org/10.1109/SUM53465.2022.9858202
74. Castro-Camus E et al. *Appl. Phys. Lett.* **86** 254102 (2005)
75. Makabe H et al. *Opt. Express* **15** 11650 (2007)
76. Li X, Jarrahi M *2020 IEEE MTT-S Int. Microwave Symp.* 91 (2020) https://doi.org/10.1109/IMS30576.2020.9224022
77. Henri R et al. *IEEE Access* **9** 117691 (2021)
78. Guerboukha H et al. *Proc. SPIE* **PC11975** PC1197502 (2022) https://doi.org/10.1117/12.2612076
79. Ponomarev D S et al. *Tech. Phys. Lett.* **48** (12) 8 (2022); *Pis'ma Zh. Tekh. Fiz.* **48** (23) 11 (2022) http://dx.doi.org/10.21883/PJTF.2022.23.53944.19332
80. Zenchenko N V et al. *Russian Technological J.* **11** (2) 50 (2023)
81. Jarrahi M *IEEE Trans. Terahertz Sci. Technol.* **5** 391 (2015)
82. Lepeshov S et al. *Laser Photon. Rev.* **11** 1600199 (2017)
83. Yachmenev A E et al. *Opt. Eng.* **59** 061608 (2019)
84. Ebbesen T W et al. *Nature* **391** 667 (1998)
85. Yardimci N T, Turan D, Jarrahi M *APL Photon.* **6** 080802 (2021)
86. Ponomarev D S et al. *Opt. Lett.* **47** 1899 (2022)
87. Lepeshov S et al. *Sci. Rep.* **8** 6624 (2018)
88. Berry C W et al. *Nat. Commun.* **4** 1622 (2013)
89. Ponomarev D S et al. *Opt. Lett.* **48** 1220 (2023)
90. Lavrukhin D V et al. *AIP Adv.* **9** 015112 (2019)
91. Li X, Yardimci N T, Jarrahi M *AIP Adv.* **7** 115113 (2017)
92. Berry C W, Hashemi M R, Jarrahi M *Appl. Phys. Lett.* **104** 081122 (2014)
93. Lu P-K, Turan D, Jarrahi M *Opt. Express* **28** 26324 (2020)
94. Nika D L et al. *Appl. Sci.* **9** 1442 (2019)
95. Zhao Z et al. *Plasmonics* **15** 263 (2020)
96. Aieta F et al. *Nano Lett.* **12** 4932 (2012)
97. Jahani S, Jacob Z *Nat. Nanotechnol.* **11** 23 (2016)
98. Mitrofanov O et al. *APL Photon.* **3** 051703 (2018)
99. Siday T et al. *Nano Lett.* **19** 2888 (2019)
100. Wang K et al. *Opt. Express* **28** 19144 (2020)
101. Khorshidi M, Dadashzadeh G *J. Infrared Millim. Terahertz Waves* **38** 609 (2017)
102. Cheng C et al. *Appl. Sci.* **9** 2524 (2019)
103. Ren D et al. *Opt. Lett.* **44** 4666 (2019)
104. Ilyakov I E et al. *Opt. Lett.* **46** 3360 (2021)
105. Klatt G et al. *Opt. Express* **18** 4939 (2010)
106. Apostolopoulos V, Barnes M E *J. Phys. D* **47** 374002 (2014)
107. Ponomarev D S et al. *Semiconductors* **51** 509 (2017); *Fiz. Tekh. Poluprovodn.* **51** 535 (2017)
108. Trukhin V N et al. *Tech. Phys. Lett.* **48** (2) 42 (2022); *Pis'ma Zh. Tekh. Fiz.* **48** (3) 51 (2022)
109. Hwang J-S et al. *Opt. Express* **15** 5120 (2007)
110. Trukhin V N et al. *Appl. Phys. Lett.* **106** 252104 (2015)
111. Trukhin V N et al. *Semiconductors* **50** 1561 (2016); *Fiz. Tekh. Poluprovodn.* **50** 1587 (2016)
112. Johnston M B et al. *Phys. Rev. B* **65** 165301 (2002)
113. Bacon D R et al. *Opt. Express* **28** 17219 (2020)
114. Du Y et al. *J. Mater. Sci. Mater. Electron.* **32** 6425 (2021)
115. Singh A et al. *ACS Photon.* **5** 2718 (2018)
116. Darrow J T et al. *IEEE J. Quantum Electron.* **28** 1607 (1992)
117. Kim D S, Citrin D S *Appl. Phys. Lett.* **88** 161117 (2006)
118. Erskine D J, Taylor A J, Tang C L *Appl. Phys. Lett.* **45** 1209 (1984)
119. Benjamin S D, Othonos A, Smith P W E *Electron. Lett.* **30** 1704 (1994)
120. Benjamin S D et al. *Appl. Phys. Lett.* **68** 2544 (1996)
121. Truchin V N, Andrianov A V, Zinov'ev N N *Phys. Rev. B* **78** 155325 (2008)
122. Cohen M L, Chelikowsky J R *Electronic Structure and Optical Properties of Semiconductors* (Springer Ser. in Solid-State Sciences, Vol. 75) (Berlin: Springer-Verlag, 1988)
123. Požela J, Reklaitis A *Solid-State Electron.* **23** 927 (1980)
124. Dong C et al. *Multi-Energy Appl. Sci.* **10** 7 (2019)
125. Alfaro-Gomez M, Castro-Camus E *Appl. Phys. Lett.* **110** 042101 (2017)
126. Dreyhaupt A et al. *Appl. Phys. Lett.* **86** 121114 (2005)
127. Park S-G et al. *IEEE J. Quantum Electron.* **35** 1257 (1999)
128. Rodriguez G, Caceres S R, Taylor A J *Opt. Lett.* **19** 1994 (1994)
129. Dekorsy T et al. *Phys. Rev. B* **47** 3842 (1993)
130. Jepsen P U, Jacobsen R H, Keiding S R *J. Opt. Soc. Am. B* **13** 2424 (1996)
131. Piao Z, Tani M, Sakai K *Jpn. J. Appl. Phys.* **39** 96 (2000)
132. Castro-Camus E, Lloyd-Hughes J, Johnston M B *Phys. Rev. B* **71** 195301 (2005)
133. Emadi R, Safian R, Nezhad A Z *IEEE J. Select. Top. Quantum Electron.* **23** 8400309 (2017) https://doi.org/10.1109/JSTQE.2016.2616448
134. Saeedkia D, Safavi-Naeini S *IEEE Photon. Technol. Lett.* **18** 1457 (2006)
135. Saeedkia D, Safavi-Naeini S *J. Lightwave Technol.* **26** 2409 (2008)
136. Lisauskas A et al. *Appl. Phys. Lett.* **98** 091103 (2011)
137. Preu S et al. *J. Appl. Phys.* **109** 061301 (2011)
138. Lu P-K et al. *Nanophotonics* **11** 2661 (2022)
139. Xu L et al. *Appl. Phys. Lett.* **59** 3357 (1991)
140. Xu L et al. *Appl. Phys. Lett.* **62** 3507 (1993)
141. Ishibashi T et al., in *Ultrafast Electronics and Optoelectronics, Technical Digest, March 17–19, 1997, Incline Village, Nevada* (Washington, DC: Optical Society of America, 1997) p. UC3
142. Ishibashi T et al. *Jpn. J. Appl. Phys.* **36** 6263 (1997)
143. Ishibashi T, Ito H *J. Appl. Phys.* **127** 031101 (2020)
144. Ito H et al. *Semicond. Sci. Technol.* **20** S191 (2005)
145. Wun J-M et al., in *Optical Fiber Communications Conf. and Exhibition, OFC, 22–26 March 2015, Los Angeles, CA, USA* (Washington, DC: Optical Society of America, 2015) p. M3C.6
146. Döhler G H et al. *Semicond. Sci. Technol.* **20** S178 (2005)
147. Preu S et al. *Appl. Phys. Lett.* **90** 212115 (2007)
148. Auston D, Glass A M, Ballman A A *Phys. Rev. Lett.* **28** 897 (1972)
149. Leitenstorfer A et al. *Appl. Phys. Lett.* **74** 1516 (1999)
150. Hu B B et al. *Appl. Phys. Lett.* **56** 506 (1990)
151. Ilyakov I E et al. *Opt. Lett.* **42** 1704 (2017)
152. Huang W R et al. *J. Mod. Opt.* **62** 1486 (2015)
153. Nagai M et al. *Appl. Phys. Lett.* **85** 3974 (2004)
154. Huber R et al. *Appl. Phys. Lett.* **76** 3191 (2000)
155. Wilke I, Sengupta S "Nonlinear optical techniques for terahertz pulse generation and detection optical rectication and electrooptic sampling," in *Terahertz Spectroscopy: Principles and Applications* (Ed. S L Dexheimer) (Boca Raton, FL: CRC Press, 2008) Ch. 2
156. Hauri C P et al. *Appl. Phys. Lett.* **99** 161116 (2011)
157. Jazbinsek M et al. *Appl. Sci.* **9** 882 (2019)
158. Esaulkov M et al. *Optica* **2** 790 (2015)
159. Clough B, Dai J, Zhan X-C *Mater. Today* **15** 50 (2012)
160. Thomson M D, Blank V, Roskos H G *Opt. Express* **18** 23173 (2010)
161. Dai J, Liu J, Zhang X-C *IEEE J. Select. Top. Quantum Electron.* **17** 183 (2011)
162. Hamster H et al. *Phys. Rev. Lett.* **71** 2725 (1993)
163. Dai J et al. *IEEE Trans. Terahertz Sci. Technol.* **1** 274 (2011)
164. Dai J, Xie X, Zhang X-C *Phys. Rev. Lett.* **97** 103903 (2006)
165. Hu B B, Nuss M C *Opt. Lett.* **20** 1716 (1995)
166. Amenabar I, Lopez F, Mendikute A *J. Infrared Millim. Terahertz Waves* **34** 152 (2013)
167. Zhong S *Front. Mech. Eng.* **14** 273 (2019)
168. True J et al. *Opt. Eng.* **60** 060901 (2021)
169. Jördens C et al. *Polymer Testing* **29** 209 (2010)
170. Park S-H, Jang J-W, Kim H-S *J. Micromech. Microeng.* **25** 095007 (2015)
171. Ryu C-H et al. *Compos. Struct.* **156** 338 (2016)
172. Oh G-H et al. *Compos. Sci. Technol.* **157** 67 (2018)
173. Charron D M et al. *Anal. Chem.* **85** 1980 (2013)
174. Ding L et al. *J. Appl. Spectrosc.* **85** 1143 (2019)
175. Shi L et al. *J. Mol. Model.* **26** 25 (2020)
176. Cherkasova O P et al. *Opt. Spectrosc.* **128** 855 (2020); *Optika i Spektroskopiya* **128** 852 (2020)
177. Zaytsev K I et al. *J. Opt.* **22** 013001 (2020)
178. Nikitkina A I et al. *J. Biomed. Opt.* **26** 043005 (2021)

179. Chen X et al. *Chem. Phys. Rev.* **3** 011311 (2022)
180. Zhang X-C *Phys. Med. Biol.* **47** 3667 (2002)
181. Busch S et al. *Opt. Lett.* **37** 1391 (2012)
182. Yee D-S et al. *Opt. Express* **23** 5027 (2015)
183. Zanotto L et al. *Opto-Electron. Adv.* **3** 200012 (2020)
184. Nemoto N et al. *IEEE Trans. Terahertz Sci. Technol.* **6** 175 (2016)
185. Zolliker P et al. *Sensors* **21** 3757 (2021)
186. Yang J, Ruan S, Zhang M *Chin. Opt. Lett.* **6** 29 (2008)
187. Jiang Z, Zhang X-C *IEEE Trans. Microwave Theory Tech.* **47** 2644 (1999)
188. Al Hadi R et al. *IEEE J. Solid-State Circuits* **47** 2999 (2012)
189. Smye S W et al. *Phys. Med. Biol.* **46** R101 (2001)
190. Katletz S et al. *Opt. Express* **19** 23042 (2011)
191. Roussel E et al. *Light Sci. Appl.* **11** 14 (2022)
192. Augustin S et al. *Sci. Rep.* **8** 4886 (2018)
193. Donoho D L *IEEE Trans. Inform. Theory* **52** 1289 (2006)
194. Candes E J, Romberg J, Tao T *IEEE Trans. Inform. Theory* **52** 489 (2006)
195. Chan W L et al. *Appl. Phys. Lett.* **93** 121105 (2008)
196. Stantchev R I et al. *Nat. Commun.* **11** 2535 (2020)
197. Minsky M *Scanning* **10** (4) 128 (1988) https://doi.org/10.1002/sca.4950100403
198. Zinov'ev N N et al. *JETP Lett.* **88** 492 (2008); *Pis'ma Zh. Eksp. Teor. Fiz.* **88** 567 (2008)
199. Salhi M A, Pupeza I, Koch M *J. Infrared Millim. Terahertz Waves* **31** 358 (2010) https://doi.org/10.1007/s10762-009-9590-7
200. Siciliani De Cumis U et al. *Opt. Exp.* **20** 21924 (2012)
201. Li Q et al. *J. Opt. Soc. Am. A* **33** 637 (2016)
202. Nguyen Pham H H et al. *APL Photon.* **2** 056106 (2017)
203. Luk'yanchuk B S et al. *Opt. Mater. Express* **7** 1820 (2017)
204. Minin I V, Minin O V *Opt. Quantum Electron.* **49** 326 (2017)
205. Yu T et al. *Opt. Commun.* **459** 124896 (2020)
206. Zaytsev K I et al. *Opt. Eng.* **52** 068203 (2013)
207. Lash A A, Yundev D N *Int. J. Infrared Millim. Waves* **5** 489 (1984)
208. Zhang X-C *Philos. Trans. R. Soc. A* **362** 283 (2004)
209. Mittleman D M et al. *Opt. Lett.* **22** 904 (1997)
210. Yakovlev E V et al. *IEEE Trans. Terahertz Sci. Technol.* **5** 810 (2015)
211. Zhong H et al. *IEEE Sensors J.* **5** 203 (2005)
212. Takayanagi J et al. *Opt. Express* **17** 7533 (2009)
213. Zhai M et al. *J. Infrared Millim. Terahertz Waves* **41** 926 (2020)
214. Ólafsson G, Quinto E T (Eds) *The Radon Transform, Inverse Problems, and Tomography: American Mathematical Society Short Course, January 3–4, 2005, Atlanta, Georgia* (Proc. of Symp. in Applied Mathematics, Vol. 63) (Providence, RI: American Mathematical Society, 2006)
215. Otani J, Mukunoki T, Obara Y *Soils Found.* **40** 111 (2000)
216. Ferguson B et al. *Opt. Lett.* **27** 1312 (2002)
217. Brahm A et al. *Appl. Phys. B* **100** 151 (2010)
218. Shibuya T et al. *J. Infrared Millim. Terahertz Waves* **32** 716 (2011)
219. Jewariya M et al. *Opt. Express* **21** 2423 (2013)
220. Hung Y-C et al. *Opt. Express* **30** 22523 (2022)
221. Lecun Y et al. *Proc. IEEE* **86** 2278 (1998)
222. Zhenwei Z et al. *Front. Phys.* **10** 893145 (2022)
223. Hunsche S et al. *Opt. Commun.* **150** 22 (1998)
224. Hunsche S et al. *IEICE Trans. Electron.* **E81-C** (2) 269 (1998)
225. Mair S, Gompf B, Dressel M *Appl. Phys. Lett.* **84** 1219 (2004)
226. Mitrofanov O et al. *IEEE J. Select. Top. Quantum Electron.* **7** 600 (2001)
227. Mitrofanov O et al. *IEEE Trans. Terahertz Sci. Technol.* **6** 382 (2016)
228. Giordano M C et al. *Optica* **5** 651 (2018)
229. Eisele M et al. *Nat. Photon.* **8** 841 (2014)
230. Chen H-T et al. *Phys. Rev. Lett.* **93** 267401 (2004)
231. Huber A J et al. *Nano Lett.* **8** 3766 (2008)
232. Kumar N et al. *Opt. Express* **20** 11277 (2012)
233. Blanchard F et al. *Opt. Express* **20** 19395 (2012)
234. Bhattacharya A, Gómez Rivas J *APL Photon.* **1** 086103 (2016)
235. Bitzer A et al. *Opt. Express* **19** 2537 (2011)
236. Betzig E et al. *Science* **251** 1468 (1991)
237. Betzig E, Finn P L, Weiner J S *Appl. Phys. Lett.* **60** 2484 (1992)
238. Keilmann F *Infrared Phys. Technol.* **36** 217 (1995)
239. Bethe H A *Phys. Rev.* **66** 163 (1944)
240. Bouwkamp C J *Philips Res. Rep.* **5** 321 (1950)
241. Mitrofanov O et al. *Appl. Phys. Lett.* **77** 3496 (2000)
242. Chen Q et al. *Opt. Lett.* **25** 1122 (2000)
243. Macfaden A J et al. *Appl. Phys. Lett.* **104** 011110 (2014)
244. Bansal R (Ed.), Sadiku M N O et al. (Contrib.) *Fundamentals of Engineering Electromagnetics* (Boca Raton, FL: CRC Press, 2006)
245. Zhan H, Mendis R, Mittleman D M *Opt. Express* **18** 9643 (2010)
246. Mitrofanov O, Renaud C C, Seeds A J *Opt. Express* **20** 6197 (2012)
247. Liu S, Mitrofanov O, Nahata A *Opt. Express* **24** 2728 (2016)
248. Wang N, Chang T, Cui H-L *Appl. Opt.* **60** 6308 (2021)
249. Mitrofanov O et al. *ACS Photon.* **2** 1763 (2015)
250. Mitrofanov O et al. *Sci. Rep.* **7** 44240 (2017)
251. Zenhausern F, O'Boyle M P, Wickramasinghe H K *Appl. Phys. Lett.* **65** 1623 (1994)
252. Zenhausern F, Martin Y, Wickramasinghe H K *Science* **269** 1083 (1995)
253. van der Valk N C J, Planken P C M *Appl. Phys. Lett.* **81** 1558 (2002)
254. Chen H-T, Kersting R, Cho G C *Appl. Phys. Lett.* **83** 3009 (2003)
255. Cho G C et al. *Semicond. Sci. Technol.* **20** S286 (2005)
256. von Ribbeck H-G et al. *Opt. Express* **16** 3430 (2008)
257. Knoll B, Keilmann F *Opt. Commun.* **182** 321 (2000)
258. Adam A J L, van der Valk N C J, Planken P C M *J. Opt. Soc. Am. B* **24** 1080 (2007)
259. Cvitkovic A, Ocelic N, Hillenbrand R *Opt. Express* **15** 8550 (2007)
260. Moon K et al. *Opt. Express* **19** 11539 (2011)
261. Moon K et al. *Appl. Phys. Lett.* **101** 011109 (2012)
262. Trukhin V N, Samoxlov L L, Khor'kov D P *JETP Lett.* **96** 807 (2013); *Pis'ma Zh. Eksp. Teor. Fiz.* **96** 899 (2012)
263. Trukhin V N et al. *JETP Lett.* **93** 119 (2011); *Pis'ma Zh. Eksp. Teor. Fiz.* **93** 134 (2012)
264. Alekseev P A et al. *Tech. Phys. Lett.* **46** 756 (2020); *Pis'ma Zh. Tekh. Fiz.* **46** (15) 29 (2020)
265. Chen X et al. *ACS Photon.* **7** 687 (2020)
266. Pizzuto A et al. *Opt. Express* **29** 15190 (2021)
267. Pogna E A A et al. *APL Photon.* **6** 061302 (2021)
268. Richter W, Becker C R *Phys. Status Solidi B* **84** 619 (1977)
269. Yang Z et al. *Small* **17** 2005814 (2021)
270. Qiu F et al. *iScience* **25** 104637 (2022)
271. Thomas L et al. *ACS Appl. Mater. Interfaces* **14** 32608 (2022)
272. Stantchev R I et al. *Sci. Adv.* **2** (6) e1600190 (2016)
273. Stantchev R I et al. *Optica* **4** 989 (2017)
274. Mansfield S M, Kino G S *Appl. Phys. Lett.* **57** 2615 (1990)
275. Terris B D et al. *Appl. Phys. Lett.* **65** 388 (1994)
276. Chernomyrdin N V et al. *Appl. Phys. Lett.* **110** 221109 (2017)
277. Choi D-H et al. *Sensors* **21** 6990 (2021)
278. Chernomyrdin N V et al. *Appl. Phys. Lett.* **113** 111102 (2018)
279. Chernomyrdin N V et al. *Appl. Phys. Lett.* **120** 110501 (2022)
280. Chernomyrdin N V et al. *Opt. Eng.* **59** 061605 (2019)
281. Ma D et al. *Appl. Opt.* **61** 7861 (2022)
282. Chernomyrdin N V et al. *Opt. Spectrosc.* **126** 560 (2019); *Optika i Spektroskopiya* **126** 642 (2019)
283. Kucheryavenko A S et al. *Biomed. Opt. Express* **12** 5272 (2021)
284. Chernomyrdin N V et al. *Opto-Electron. Adv.* **6** 220071 (2023)
285. Chernomyrdin N V et al. *Optica* **8** 1471 (2021)
286. Zhelnov V A et al. *Opt. Express* **29** 3553 (2021)
287. Chapdelaine Q et al. *Opt. Mater. Express* **12** 3015 (2022)